



# High spatial resolution monitoring land surface energy, water and CO<sub>2</sub> fluxes from an Unmanned Aerial System



Sheng Wang<sup>a,\*</sup>, Monica Garcia<sup>a,f,\*</sup>, Peter Bauer-Gottwein<sup>a</sup>, Jakob Jakobsen<sup>b</sup>, Pablo J. Zarco-Tejada<sup>c,d,e</sup>, Filippo Bandini<sup>a</sup>, Verónica Sobejano Paz<sup>a</sup>, Andreas Ibrom<sup>a</sup>

<sup>a</sup> Department of Environmental Engineering, Technical University of Denmark, 2800 Kgs. Lyngby, Denmark

<sup>b</sup> National Space Institute, Technical University of Denmark, 2800 Kgs. Lyngby, Denmark

<sup>c</sup> Department of Infrastructure Engineering, Melbourne School of Engineering, University of Melbourne, Melbourne, Victoria, Australia

<sup>d</sup> School of Agriculture and Food, Faculty of Veterinary and Agricultural Sciences, University of Melbourne, Melbourne, Victoria, Australia

<sup>e</sup> Instituto de Agricultura Sostenible (IAS), Consejo Superior de Investigaciones Científicas (CSIC), Córdoba, Spain

<sup>f</sup> International Research Institute for Climate and Society, The Earth Institute, Columbia University, Palisades, NY, USA

## ARTICLE INFO

### Keywords:

Evapotranspiration  
Gross primary productivity  
Eddy covariance  
Optical and thermal remote sensing  
Instantaneous and diurnal  
Spatial heterogeneity

## ABSTRACT

High spatial resolution maps of land surface energy, water and CO<sub>2</sub> fluxes, e.g. evapotranspiration (ET) and gross primary productivity (GPP), are important for agricultural monitoring, ecosystem and water resources management. However, it is not clear which is the optimal (e.g. coarsest possible) spatial resolution to capture those fluxes accurately. Unmanned Aerial Systems (UAS) can address this by collecting very high spatial resolution (< 1 m, VHR) imagery. The objective of this study is to model ET and GPP dynamics using VHR optical and thermal imagery and quantify the influence of the spatial heterogeneity in the flux simulations and validations. The study was conducted at a deciduous willow bioenergy eddy covariance (EC) flux site in Denmark. Flight campaigns were conducted during the growing seasons of 2016 and 2017 with a hexacopter equipped with RGB, multispectral and thermal infrared cameras. A 'top-down' modeling approach consisting of the Priestley–Taylor Jet Propulsion Laboratory model and a light use efficiency model sharing the same canopy biophysical constraints was used to estimate ET and GPP. Model outputs were benchmarked by EC flux observations with the source weighted footprint. Our results indicate that our model can well estimate the instantaneous net radiation, ET, GPP, evaporative fraction, light use efficiency and water use efficiency with root-mean-square deviations (RMSD) of 31.6 W·m<sup>-2</sup>, 41.2 W·m<sup>-2</sup>, 3.12 μmol·C·m<sup>-2</sup>·s<sup>-1</sup>, 0.08, 0.16 g·C·MJ<sup>-1</sup> and 0.35 g·C·kg<sup>-1</sup>, respectively. Further, it is found that using a footprint model to sample different areas of VHR imagery can be a tool to provide better diurnal estimates to benchmark with EC data. Moreover, these VHR maps (0.3 m) allowed us to quantify metrics of spatial heterogeneity by using semivariogram analysis and by aggregating model inputs into different spatial resolutions. For instance, we find that in this site, the aggregation of simulated GPP using the source weighted mean of the EC footprint was about 30% lower in RMSD than using the arithmetic mean of the footprint. This demonstrates the accuracy of the modeled VHR spatial patterns. Nevertheless, we also find that imagery resolution consistent with the canopy size (around 1.5 m in our study) is sufficient to capture the spatial heterogeneity of the fluxes as transpiration and canopy assimilation of CO<sub>2</sub> are processes regulated at the tree crown level. Our results highlight the importance of considering the land surface heterogeneity for flux modeling and the source contribution within the EC footprint for model benchmarking at appropriate spatial resolutions.

## 1. Introduction

The amount of carbon assimilated by terrestrial ecosystems or gross primary productivity (GPP) is closely connected to the water loss as evapotranspiration (ET), as both processes are regulated by a variety of linked biotic and abiotic controls (Damm et al., 2018; Foley et al., 1996;

Guan et al., 2015). This tradeoff between GPP and ET requires strategies and policies for management and monitoring of water, crops and natural ecosystems (Liu et al., 2015; Mo et al., 2018). Quantification of the temporal and spatial variations of ET and GPP can provide valuable information for understanding the water and carbon exchanges between land surfaces and the atmosphere in a changing climate (Beer

\* Corresponding authors.

E-mail addresses: [shengwang12@gmail.com](mailto:shengwang12@gmail.com) (S. Wang), [mgarc@env.dtu.dk](mailto:mgarc@env.dtu.dk) (M. Garcia).

<https://doi.org/10.1016/j.rse.2019.03.040>

Received 18 June 2018; Received in revised form 4 February 2019; Accepted 30 March 2019

0034-4257/ © 2019 Elsevier Inc. All rights reserved.

et al., 2010; Ito and Inatomi, 2012). Very high spatial resolution (VHR, < 1 m) maps are particularly important for optimizing food or bioenergy crop production. For example, targeted irrigation or fertilization in precision agriculture will benefit from VHR water use efficiency (WUE) maps, reflecting the amount of carbon fixed per unit of water transpired, but such information is not yet routinely available (Gago et al., 2015). Further, VHR maps offer great opportunities to understand ecohydrological processes and to reduce the large uncertainty in the estimation of land surface fluxes due to unresolved scaling issues (Anderson and Gaston, 2013; Vivoni et al., 2014).

Numerous methods such as the eddy covariance (EC) technique, satellite and airborne remote sensing, and land surface models have been developed to estimate land surface energy, water and CO<sub>2</sub> fluxes across leaf, canopy, regional and global scales (Amthor et al., 2001; Reichstein et al., 2005; Sitch et al., 2003). Among them, the EC technique is acknowledged as one of the reliable methods to estimate the exchange of tracer gases (e.g. CO<sub>2</sub> and water vapor) between the land surface and the atmosphere at the ecosystem level (Baldocchi, 2003). It is often used to benchmark models. However, the EC technique can only be applied in flat and homogeneous sites and the footprint of the measurements usually covers areas around 100–1000 m<sup>2</sup>. To estimate the spatial variation of regional ET and GPP, models using satellite optical and thermal remote sensing data are a cost-effective tool. However, the coarse spatial resolutions of satellite optical and thermal imagery cannot represent the spatial heterogeneity in topography, soils, and vegetation accurately enough (McCabe et al., 2017). Further, the coarse pixel resolution of satellite ET and GPP products, e.g. MODIS (250 m–1 km), Sentinel 2 missions (10 m–60 m) or the Sentinel 3 missions (500 m–1 km), may not be appropriate for small-scale applications, e.g. irrigation management in vineyards. Additionally, during cloudy and overcast weather conditions, satellites are not able to provide optical or thermal observations of the land surface. This is an important issue especially for high latitude regions, where cloudy and overcast days are common (Wang et al., 2018b) or in climates where the growing season coincides with the rainy season such as monsoonal regimes (García et al., 2013).

With significant advances in navigation, flight control, miniaturized platforms and sensors, Unmanned Aerial Systems (UAS) can provide VHR imagery, presenting unprecedented potential for monitoring ecohydrological processes at fine scales (Vivoni et al., 2014). VHR remote sensing data can facilitate our understanding of the heterogeneity and scaling uncertainties in the ecohydrological processes (Li et al., 2013). Besides, UAS flight campaigns can be conducted at flexible times, locations and turnaround times. The flexibility to combine various sensors and to design different flight paths is another advantage of UAS. Further, UAS can collect data under both sunny and cloudy weather conditions. Additionally, the operating costs of UAS campaigns are much lower than manned airborne surveys.

Recent studies have demonstrated that UAS remote sensing is able to produce good estimates of ET with the root-mean-square-deviation (RMSD) around 10–30% of the measured fluxes over irrigated crops (Hoffmann et al., 2016; Kustas et al., 2018; Ortega-Farías et al., 2016) and grasslands (Brenner et al., 2017). Most of them focused on using thermal approaches based on models of the Two Source Energy Balance (TSEB) family to calculate sensible heat flux and estimated ET as the residual component of the surface energy balance (Kustas and Norman, 1999). However, sensible heat estimates are very dependent on the accuracy of radiometric temperature, which is quite low in the case of the typically miniaturized uncooled thermal cameras on board of UAS (Wang et al., 2018a). An alternative of ET estimation is vegetation-driven approaches, e.g. Priestley–Taylor Jet Propulsion Laboratory model (PT-JPL, Fisher et al., 2008), which are less sensitive to the quality of radiometric temperature (García et al., 2013).

Compared to ET, reports on GPP and WUE estimates from UAS imagery are even scarcer. Studies usually do not estimate GPP and WUE directly but proxies such as stomatal conductance, pigments or leaf area

index (LAI). For instance, Zarco-Tejada et al. (2013b) demonstrated chlorophyll fluorescence, physiological indices (e.g. photochemical reflectance index, PRI), and structural indices (e.g. normalized difference vegetation index, NDVI) and enhanced vegetation index derived from UAS observations correlate well with EC CO<sub>2</sub> fluxes. Furthermore, to calculate ecosystem WUE and compare estimates of water and CO<sub>2</sub> fluxes with other approaches (e.g. EC techniques), it is necessary to give quantitative estimates of GPP and ET.

Models of ET and GPP for routine UAS monitoring should be operational and parsimonious with limited parameterization and data inputs (ideally all data inputs from UAS). Remote sensing satellite models for joint ET and GPP estimation can be classified into ‘top-down’ and ‘bottom-up’ approaches (Houborg et al., 2009; Wang et al., 2018b). ‘Top-down’ methods, e.g. CASA light use efficiency (LUE) model (Potter et al., 1993), the MODIS GPP and ET algorithms (Mu et al., 2007; Running et al., 2004) or PT-JPL (Fisher et al., 2008), are simpler and can be directly driven with remote sensing imagery. The ‘top-down’ models treat ecological behavior of the canopy as a whole and estimate the actual status of ecosystem functioning by reduction from the potential status with various environmental constraints. One example is the joint PT-JPL model and LUE model, which unified the two often used ‘top-down’ ET and GPP models with the same environmental constraints and has been demonstrated to successfully simulate ET and GPP dynamics in a temperate deciduous forest (Wang et al., 2018b).

The temporal upscaling of land surface fluxes from the instantaneous to the diurnal and model benchmarking with EC measurements are important issues (Chen et al., 1999; Gentine et al., 2007; Kim et al., 2006; Morillas et al., 2014). Due to the particle dispersion process, areas within the footprint contribute differently to EC measurements depending on various factors, e.g. the distance between source areas and sensors, sensor height, canopy height, surface roughness, wind speed and variance (Metzger, 2018). Traditionally, the coarse resolution satellite imagery cannot assess the importance of considering the variations of the EC footprint in the model benchmarking with EC measurements. The VHR imagery provides explicit information on surface conditions matching the variability of EC footprint during the course of the day. Regarding ET, most of the studies deal with the diurnal simulation by assuming the self-preservation of EF (the constant daily EF) in the diurnal evolution of the surface energy budget (Brutsaert and Sugita, 1992; P. D. Colaizzi et al., 2006). Another approach is to consider the spatial heterogeneity and variations of the EC footprints and average all instantaneous estimates during the course of the day. A key part for proper model validation is to sample different regions from the UAS imagery that change during the course of a day to address the variations of EC footprints. This kind of analysis can also improve our understanding of diurnal upscaling processes.

Despite the virtually unlimited potential of UAS to provide centimeter-level VHR data, the necessity for spatial detail depends on the purpose of the study and site conditions. For example, detecting plant diseases would require a higher spatial resolution than mapping the spatial variability of transpiration across canopies. Further, there is a tradeoff between image spatial resolution and coverage. Flying UAS at a low altitude can obtain VHR images but small coverage and vice versa. Low flying height requires more images or flights to cover the target area and leads to lower efficiency of UAS campaigns. Thus, optimizing spatial resolution and flying height for UAS campaigns is important. To achieve that, a first step to design the spatial resolution for observing missions is to characterize the landscape spatial heterogeneity (Garrigues et al., 2006). The semivariogram, which measures spatial interdependence between observations as a function of their distance, has been often adopted to quantify the heterogeneity of the land surface (Curran, 1988; Kim et al., 2006).

Understanding the influence of landscape heterogeneity on the scaling behavior of surface fluxes with different spatial resolutions is critical (McCabe and Wood, 2006; Sharma et al., 2016). Spatial scaling experiments that resample model inputs to compare simulated land

surface fluxes with EC observations is an efficient approach to quantify the influence of spatial resolutions on the modeling performance (Ershadi et al., 2013). Besides the heterogeneity of landscapes, VHR maps of land surface fluxes also enable to consider the heterogeneity of source contribution within the EC footprint. Additionally, few studies have resources to spatially validate the fluxes with numerous in-situ sensors (Kustas et al., 2018). For spatial validation, some studies compare UAS based stress indicator with in-situ measurements, e.g. stomatal conductance and leaf water potential, but there is a potential mismatch between image at canopy scale and measurements at leaf scale (Gago et al., 2015; Zarco-Tejada et al., 2013b). We hypothesize that if the spatial patterns of simulated surface fluxes from UAS imagery are not accurate, model performance will not change with the different aggregation methods (arithmetic or weighted means of the source contribution) within the EC footprint. This comparison with different aggregation methods can provide evidence of the accuracy of the spatial patterns mapped from UAS to some extent.

The overall objective of this study is to develop and validate an operational methodology for mapping land surface energy, ET, GPP and WUE at an optimal spatial resolution. Specific objectives include: 1) to propose an operational methodology using UAS optical and thermal imagery with minimum ground observations to map land surface fluxes, 2) to quantify the accuracy of the simulated instantaneous and diurnal land surface variables with EC observations and assess the importance of considering variations of the EC footprint in the temporal upscaling from the instantaneous to the diurnal, and 3) to evaluate the influence of heterogeneity and spatial resolution on the flux simulations and identify the optimum spatial resolution to benchmark models with EC tower observations.

## 2. Study site and in-situ data

This study was conducted in an 11 ha short rotation coppice (SRC) willow bioenergy plantation EC site. This site is located at Risoe, Denmark (DK-RCW) with latitude 55°41'31.95"N, longitude 12°6'14.69"E and altitude 15 m above mean sea level. This site is temperate maritime climate with a mean annual temperature of 8.5 °C and precipitation around 600 mm. The soil texture is loam. The willow species in the field are *Salix viminalis*, *Salix schwerinii* and *Salix triandra*. In February of 2016, all willow trees were harvested and the site was covered by bare soil before May 2016. Then willow grew to the height of approximate 4 m during growing seasons of 2016 and 2017. Rapeseed (*Brassica napus*) was grown in the nearby field (East of the SRC). A grass covered access path separates the willow plantation from the rapeseed field.

The EC observation system has employed continuously from 2012 until now. A 12 m tall mast enables EC flux measurements in the atmospheric boundary layer above the willow plantation as Fig. 1. The EC system consisted of an enclosed path CO<sub>2</sub> and H<sub>2</sub>O sensor LI-7200 (mode 177, LI-COR, Lincoln, NE, USA) and a three-dimensional ultrasonic anemometer and thermometer HS-50 (Gill Instruments, Ly-mington, UK). Turbulent flux data were recorded at 10 Hz (CR-3000 logger, Campbell, City, USA). The raw data post-processing followed the same scheme as in Pilegaard et al. (2011), Ibrom et al. (2007) and Fratini et al. (2012), i.e. the standard processing now adopted by ICOS. For EC data processing, the flux partitioning to separate GPP and respiration was done by the look-up table approach (Reichstein et al., 2005) based on the R-package REddyProc (Wutzler et al., 2018) with the half-hourly net ecosystem exchange, T<sub>a</sub> and incoming shortwave radiation (SW<sub>in</sub>) as inputs. The processed EC data, ET and GPP, were used in this study for model validation.

In-situ micrometeorological observations used for this study included radiation components, the fraction of intercepted Photosynthetically Active Radiation ( $f_{IPAR}$ ), air temperature (T<sub>a</sub>), air pressure (Pa), relative humidity (RH), soil moisture (SM), wind speed (WS) and direction (WD). A CNR4 net radiometer (Kipp & Zonen, Delft,

the Netherlands) installed at 10 m height of the EC tower continuously measured components of the surface energy balance, which include SW<sub>in</sub>, outgoing shortwave radiation (SW<sub>out</sub>), incoming longwave radiation (LW<sub>in</sub>) and outgoing longwave radiation (LW<sub>out</sub>). Photosynthetically Active Radiation (PAR) measurements were obtained from ten PAR sensors (Apogee SQ-200, Apogee Instruments Inc., Logan, USA) including one sensor to measure the incident PAR above the canopy (PAR<sub>above</sub>), one sensor to measure canopy-reflected PAR (PAR<sub>reflected</sub>) and eight sensors to measure understory PAR (PAR<sub>below</sub>). For in-situ SM measurements, field campaigns with a portable TDR probe (Field Scout TDR 300 portable moisture meter, Spectrum Technologies Inc., Plainfield, IL, USA), were conducted to measure the spatial variability of SM on 18th June 2017 as shown in Fig. 1. Fixed probes (5TM ECH2O, Decagon Inc., Pullman, WA, USA) were installed in the willow plantation to measure the temporal variability of SM.

## 3. Methods and data

### 3.1. Unmanned Aerial System and campaigns

This UAS consisted of a vehicle and a payload, as shown in Fig. 2. For the vehicle, we used an off-the-shelf DJI hexacopter Spreading Wings S900 equipped with a DJI A2 flight controller. It can carry a payload with an approximate maximum weight of 2 kg. The payload included an imaging system (multispectral, thermal infrared and Red-Green-Blue RGB cameras), a Global Navigation Satellite System (GNSS) and a Single-Board Computer (SBC) Beaglebone Black for sensor communication and data storage. Details on the GNSS onboard, refer to Bandini et al. (2018). Additionally, we used a real-time kinematic (RTK) GNSS (Trimble GNSS R8s, Trimble Inc., CA, USA) to measure ground control points (GCPs) to improve the geometric accuracy of the image mosaicking process. The imaging system included three sensors: a multispectral camera, a thermal infrared camera and an RGB camera. The multispectral camera (MCA, Multispectral Camera Array, Tetracam, Chatsworth, CA, USA) consists of an array of six individual channels for the visible and near-infrared bands, namely 470, 530, 570, 670, 710 and 800 nm with the full width at half maximum for each channel is 10 nm. The thermal infrared camera (FLIR Tau2 324, Wilsonville, OR, USA) has an uncooled VOx microbolometer. It records longwave radiation in the wavelength range from 7.5 to 13.5 μm and is able to measure temperature ranging from -25 °C to 100 °C in high gain mode. The RGB camera (Sony DSC-RX100) was used to produce the Digital Surface Model (DSM). Detailed information on sensors is shown in Table 1.

A total of eight UAS flight campaigns were conducted at the willow site during different growing stages of willow and weather conditions in 2016 and 2017 as shown in Table 2. It should be noted that during the first two flights, the EC system did not work and these two flights were only used to simulate land surface energy balance and SM, which were further compared with in-situ measurements. The flight paths (Fig. 1) were designed using the DJI autopilot software. Before each flight campaign, the FLIR thermal camera was turned on half an hour for stabilization.

### 3.2. Image processing and validation

Before image processing, thorough laboratory geometric and radiometric calibrations of imaging sensors were conducted. Geometric calibration of the RGB and multispectral cameras was conducted with standard checkerboard calibration patterns to estimate intrinsic camera geometric parameters. Radiometric calibration for each channel of MCA was conducted with an integrating sphere (ISP2000, Instrument Systems, München, Germany) and the in-lab calibration showed that the bias of the measured radiance was within ± 4.8%. For details, refer to Wang et al. (2017). FLIR was calibrated using a Landcal P80P black body radiation source (Land Instruments, Leicester, United Kingdom)

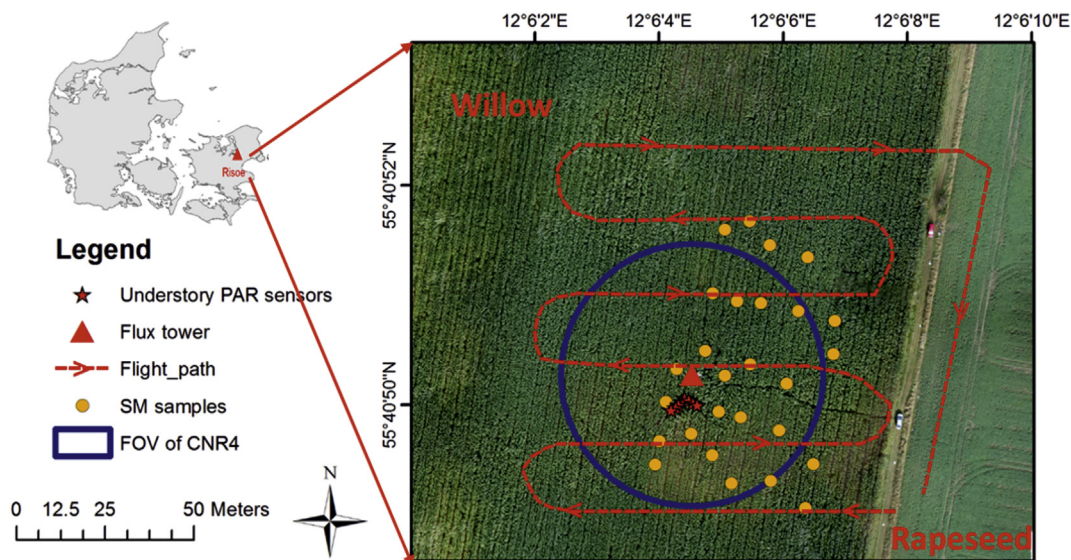


Fig. 1. Overview of Risoe EC flux site and flight paths of campaigns. The flux tower is in the middle of the willow plantation. The red dashed line shows the flying path of UAS flight campaigns. Red stars indicate the location of the understory PAR sensors. Yellow dots show the location of SM samples conducted on 18th June 2017. The blue circle indicates the field of view (FOV) of CNR4, when willow height is 0 m. (For interpretation of the references to colour in this figure legend, the reader is referred to the web version of this article.)

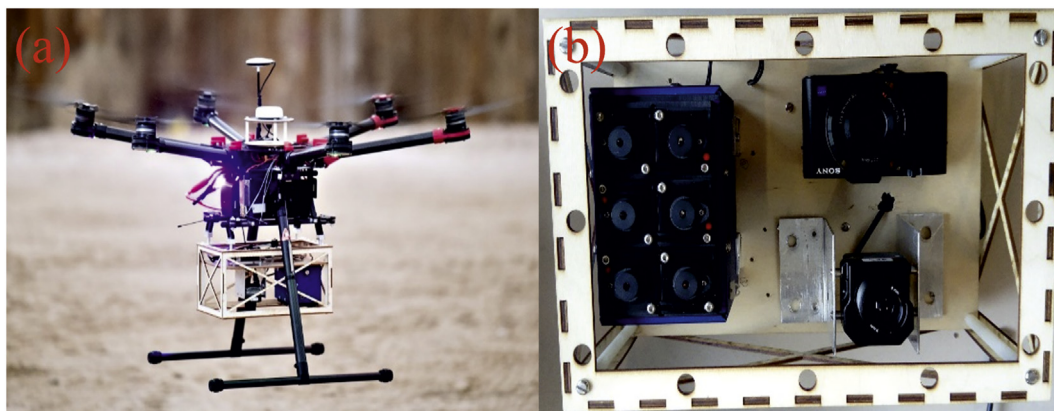


Fig. 2. (a) DJI S900 vehicle platform and (b) the payload including an RGB camera, a thermal infrared camera and a multispectral camera.

with ten different target temperatures ranging from 0 to 45 °C and three ambient temperatures ranging from 0 °C to 30 °C. This calibration resulted in in-lab accuracy RMSD of 0.50 °C with the same ambient and target temperatures and RMSD of 0.95 °C with different ambient and target temperatures (Wang et al., 2018a).

Images obtained from UAS flight campaigns were georeferenced using UAS GNSS data. Then these georeferenced images along with pre-calibrated intrinsic camera geometric parameter values were imported into Agisoft Photoscan (Agisoft LLC, St. Petersburg, Russia), which was based on the structure from motion (SfM) algorithm (Westoby et al., 2012), to generate orthophotos and DSM. After that, high accuracy GCPs were added to the aligned images and optimize the estimated camera positions and angles. The DSM generated from RGB images was imported into multispectral and thermal projects in Agisoft to aid the orthorectification of multispectral and thermal images to remove relief displacement. Finally, the generated multispectral and thermal orthophotos were converted to six band reflectance and surface brightness temperature ( $T_b$ ), respectively.

The six band reflectance was calculated based on the radiance method. The incoming solar spectral radiance ( $L_{in, \lambda}$ ) measured by a handheld spectroradiometer (ASD, FieldSpec HandHeld 2™, Analytical Spectral Devices, Inc., Boulder, USA) with a Spectralon panel (a

nominal reflectance of 99.99%) on the ground before and after each flight campaign. The averaged measurements from ASD were used as  $L_{in, \lambda}$ . The at-sensor radiance ( $L_{MCA, \lambda}$ ) collected by MCA during the flight campaigns was used to represent the reflected radiance. Due to the low flight altitude and the limited influence of atmospheric attenuation, the difference between the reflected radiance at the sensor and at the surface was neglected. With the Eq. (1), the reflectance for each band was calculated. The near-infrared (800 nm) and the red band (670 nm) reflectance were used to calculate NDVI ( $(\rho_{800} - \rho_{670}) / (\rho_{800} + \rho_{670})$ ) to infer the vegetation growth.

$$\rho_{\lambda} = \frac{L_{MCA, \lambda}}{L_{in, \lambda}} \quad (1)$$

where  $\rho_{\lambda}$  is the reflectance from MCA.  $\lambda$  is the wavelength (nm).  $L_{MCA, \lambda}$  is the reflected spectral radiance measured by MCA ( $W \cdot m^{-2} \cdot sr^{-1} \cdot nm^{-1}$ ).  $L_{in, \lambda}$  is the incoming spectral radiance measured by ASD with a Spectralon panel on the ground ( $W \cdot m^{-2} \cdot sr^{-1} \cdot nm^{-1}$ ).

To validate the accuracy of acquired UAS data, reflectance of tarpaulins with four different colors (green, blue, black and silver) was measured with the ASD for each flight. Tarpaulins are acknowledged to have low anisotropic effects (Korpela et al., 2011). The measured reflectance by ASD on the ground was used to validate reflectance

**Table 1**  
Information on optical and thermal sensors (DSM: digital surface model; NDVI: normalized difference vegetation index; T<sub>s</sub>: land surface temperature).

Camera	Focal length (mm)	Image dimension (pixel)	Field of View	Spectrum	Spatial resolution at ground when flying at 12 m <sup>a</sup>	Spatial resolution at ground when flying at 90 m <sup>b</sup>	Purpose
RGB	10.4	5472 × 3648	64.8° × 45.9°	Red, Green, Blue	0.33 cm	2.5 cm	DSM
Multispectral	9.6	1280 × 1024	38.3° × 32°	470, 530, 570, 670, 710, 800 nm	0.64 cm	4.8 cm	NDVI
Thermal	9	324 × 256	48.5° × 39.1°	0.75 μm to 13.5 μm	3.29 cm	24.7 cm	T <sub>s</sub>

<sup>a</sup> The final spatial resolution of multispectral and thermal images, which was used for modeling, was 0.03 m.

<sup>b</sup> The final resolution for modeling was 0.3 m.

obtained from MCA. The validation was shown for 670 and 800 nm, as only these bands were used to calculate NDVI as model inputs.

For thermal infrared images, the generated T<sub>b</sub> orthophotos were compared with the brightness temperature T<sub>b,CNR4</sub> converted from the outgoing longwave radiation (LW<sub>out,CNR4</sub>) from CNR4 on the tower (Eq. (2)). It should be noted that there may be uncertainties for this comparison, since FLIR and CNR4 have different thermal wavelength responses and sensor field of views (FOVs). FLIR measures longwave radiation ranging from 7.5 to 13.5 μm, while CNR4 has a broader response range and measures longwave emission from 4.5 to 45 μm. The FOV of FLIR is 35° × 27° (Table 1), while the downward FOV of CNR4 is 150°. However, this comparison was necessary and can provide insights into the quality of the thermal data to some extent. Additionally, this comparison was equivalent to the comparison between LW<sub>out,CNR4</sub> and the longwave radiation (LW<sub>out,FLIR</sub>) estimated from FLIR T<sub>b</sub>. This was important to understand uncertainties in calculating land surface energy balance components with UAS imagery. Thus LW<sub>out,CNR4</sub> was converted to brightness temperature T<sub>b,CNR4</sub> by applying Stefan Boltzmann's law as Eq. (2) to compare with T<sub>b</sub> from FLIR.

$$T_{b\_CNR4} = \left( \frac{LW_{out\_CNR4}}{\sigma} \right)^{1/4} \tag{2}$$

where σ is the Stefan-Boltzmann constant (5.67 × 10<sup>-8</sup> W·m<sup>-2</sup>·K<sup>-4</sup>). T<sub>b,CNR4</sub> is the brightness temperature (K). LW<sub>out,CNR4</sub> is the longwave radiation from CNR4 (W·m<sup>-2</sup>).

To obtain the corresponding pixels in the field of view (FOV) of CNR4, the flux tower position, FOV and sensor height of CNR4, and vegetation height (Table 2) were used to calculate the radius of the FOV areas on the ground according to Eq. (3), as one example shown in Fig. 1.

$$r = (H - h) \tan\left(\frac{FOV}{2}\right) \tag{3}$$

where r is the radius in m. H is the sensor height (10 m). h is the height of the willow ranging from 0 to 4.95 m during the study period (Table 2). FOV is the downward FOV of CNR4, namely 150°.

### 3.3. Model description

The joint ‘top-down’ PT-JPL ET and LUE GPP model (Wang et al., 2018b) was used to simulate the land surface fluxes from UAS imagery. Such a ‘top-down’ approach is based on simple scaling rules using remote sensing estimates of the fraction of absorbed radiation by canopies and requires limited model inputs and parameters. Comparisons have shown that PT-JPL routinely outperforms more sophisticated modeling schemes using both satellite data (Ershadi et al., 2014; McCabe et al., 2017) and proximal in-situ sensors (Morillas et al., 2013), but to our knowledge, the PT-JPL model has not yet been tested using UAS data. LUE models were widely applied to estimate GPP dynamics across various ecosystems at global and regional scales (Running et al., 2004). Considering model performance, complexity and operational capabilities, this joint model (Wang et al., 2018b) was selected for this study.

The ET part of this joint model comes from the PT-JPL model (Fisher et al., 2008), which is based on the Priestley and Taylor (1972) equation for potential ET and incorporates eco-physiological variables to down-regulate the potential value to the actual one. PT-JPL is a three-source evapotranspiration model including wet surface evaporation (E<sub>i</sub>), transpiration (E<sub>c</sub>) and soil evaporation (E<sub>s</sub>), as described in Eqs. (4)–(7).

$$\lambda ET = \lambda E_i + \lambda E_c + \lambda E_s \tag{4}$$

$$\lambda E_i = f_{wet} \cdot \alpha \Delta / (\Delta + \gamma) \cdot R_{nc} \tag{5}$$

$$\lambda E_c = (1 - f_{wet}) \cdot f_g \cdot f_M \cdot f_{Ta} \cdot \alpha_c \Delta / (\Delta + \gamma) \cdot R_{nc} \tag{6}$$

**Table 2**

Information on UAS flight campaigns (RH: relative humidity; Ta: air temperature; WS: wind speed at 10 m; Pa: air pressure; h is the tree height).

Date	Acquisition Time	Flying height (m)	Weather	RH (%)	Ta (°C)	WS (m s <sup>-1</sup> )	Pa (kPa)	h (m)	Growth stage
2-May-2016	14:40–14:55	12	Cloudy	51.60	15.17	6.60	101.88	0.0	Early growth
12-May-2016	10:44–10:55	12	Sunny	45.85	17.31	5.11	100.62	0.0	Early growth
25-May-2016	10:11–10:23	12	Sunny	62.67	21.05	3.30	100.89	0.0	Early growth
7-Oct-2016	11:41–11:55	90	Sunny	69.87	9.94	5.62	102.05	4.05	Dense vegetation
19-May-2017	12:07–12:19	90	Sunny	79.25	19.27	2.13	100.41	4.24	Dense vegetation
22-May-2017	10:15–10:28	90	Cloudy	70.82	14.72	2.91	101.66	4.34	Dense vegetation
26-May-2017	11:13–11:26	90	Sunny	72.56	16.72	4.47	101.54	4.45	Dense vegetation
18-Jun-2017	12:39–12:51	90	Cloudy	71.79	21.81	4.42	101.62	4.95	Dense vegetation

$$\lambda E_s = f_{SM} \cdot \alpha \Delta / (\Delta + \gamma) (R_{nc} - G) \quad (7)$$

where  $\lambda ET$  is the latent heat flux for total evapotranspiration ( $W \cdot m^{-2}$ ).  $\lambda E_i$  is the evaporation from the intercepted water ( $W \cdot m^{-2}$ ).  $\lambda E_c$  is the transpiration ( $W \cdot m^{-2}$ ).  $\lambda E_s$  is the evaporation from soil ( $W \cdot m^{-2}$ ).  $f_g$  is the green canopy fraction reflecting the proportion of active canopy.  $f_M$  is the plant moisture constraint.  $f_{Ta}$  is the air temperature constraint indicating the limitation of temperature on photosynthesis.  $f_{SM}$  is the SM constraint.  $f_{wet}$  is the relative surface wetness to partition evapotranspiration from the intercepted water and transpiration (Fisher et al., 2008). These constraints vary from 0 to 1 to account for the relative reduction of potential  $\lambda ET$  under limiting environmental conditions.  $R_{nc}$  and  $R_{ns}$  are  $R_n$  for canopy and soil, respectively. The partitioning of PAR and  $R_n$  between canopy and soil is calculated following the Beer-Lambert law (Supplemental Table S1).  $G$  is the ground heat flux and is calculated based on a ratio to the soil net radiation (Kustas and Daughtry, 1990).  $\Delta$  is the slope of saturation-to-vapor pressure curve.  $\gamma$  is the psychrometric constant.  $\alpha$  is an empirical ratio of potential evapotranspiration to equilibrium potential evapotranspiration (PT coefficient) replacing the atmospheric demand and surface resistance effects in Penman-Monteith ET equation. The suggested value for the PT-JPL model is 1.26 (Fisher et al., 2008). The supplemental Table S1 shows detailed information on the model constraints and parameters for this joint LUE GPP and PT-JPL ET model.

The GPP model shares similar features with other widely used LUE models, e.g. the MODIS algorithm (Running et al., 2004), but it also has inputs to account for the photosynthetic and transpiring proportion of the canopy (green vegetation fraction) and the plant moisture constraint based on Fisher et al. (2008).

$$GPP = \varepsilon_{max} \cdot PAR_c \cdot f_g \cdot f_M \cdot f_{Ta} \cdot f_{VPD} \quad (8)$$

where GPP is the gross primary productivity ( $\mu mol \cdot C \cdot m^{-2} \cdot s^{-1}$ ).  $\varepsilon_{max}$  is the maximum LUE ( $\mu mol \cdot C \cdot m^{-2} \cdot MJ^{-1}$ ).  $PAR_c$  is PAR intercepted by the canopy ( $MJ \cdot m^{-2} \cdot s^{-1}$ ) based on the extinction of PAR within the canopy using the Beer-Lambert law (Supplemental Table S1).  $f_g$ ,  $f_M$  and  $f_{Ta}$  are

biophysical constraints and have the same meaning as in Eq. (11).  $f_{VPD}$  is the constraint indicating the stomatal response to water vapor pressure deficit (VPD). The absorbed PAR (APAR) is equal to  $PAR_c \cdot f_g$ . All constraints range from 0 and 1 and represent the reduction of maximum GPP under limiting environmental conditions. For more details, see Supplemental Table S1 and Wang et al. (2018b).

This joint model has two parameters, maximum LUE ( $\varepsilon_{max}$ ) and optimal temperature ( $T_{opt}$ ), which need to be calibrated or extracted from look-up tables based on plant functional types. A study on long-term ET and GPP simulation based on this joint model has been applied in the nearby temperate deciduous beech forest Soroe (Wang et al., 2018b). Thus, this study used the optimized values from Soroe with  $\varepsilon_{max}$  equal to  $2.97 \text{ g} \cdot \text{C} \cdot \text{m}^{-2} \cdot \text{MJ}^{-1}$  and  $T_{opt}$  equal to  $16.51 \text{ }^\circ\text{C}$  as parameter values for this study.

Besides ET and GPP, this model can also estimate ecosystem LUE ( $\text{g} \cdot \text{C} \cdot \text{MJ}^{-1}$ ), evaporative fraction (EF, no unit) and WUE ( $\text{g} \cdot \text{C} \cdot \text{kg}^{-1}$ ) as shown in Eqs. (9)–(11). These variables provide valuable information for precision agriculture and irrigation management.

$$EF = \frac{ET}{R_n - G} \quad (9)$$

$$LUE = \frac{GPP}{APAR} \quad (10)$$

$$WUE = \frac{GPP}{ET} \quad (11)$$

#### 3.4. Model application: Instantaneous and diurnal

The detailed workflow of the model application is shown in Fig. 3. We performed two types of simulations using UAS imagery: instantaneous (at the time of flight) and diurnal (every half an hour during the daytime of the flight campaign day). The main difference between both is that in the first case the net radiation ( $R_n$ ) was estimated using UAS images, while in the diurnal simulations in-situ

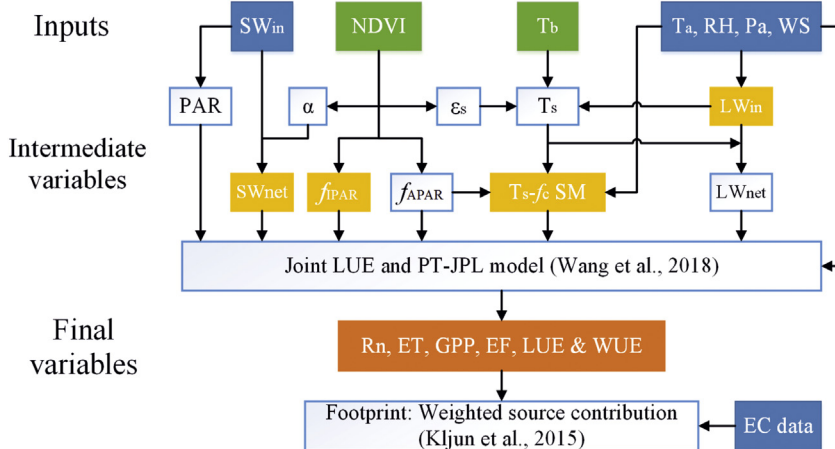


**Fig. 3.** The workflow of the instantaneous simulation. Green boxes represent inputs from UAS imagery. Blue boxes are in-situ measurements from the EC tower. Yellow boxes belong to the simulated intermediated variables. Orange boxes are the simulated final variables. Variables in green, yellow and orange boxes were validated by in-situ measurements. (For interpretation of the references to colour in this figure legend, the reader is referred to the web version of this article.)

measurements of Rn were used. For the instantaneous simulation, inputs from UAS imagery are shown in the green boxes of Fig. 3. Meteorological inputs for modeling included  $SW_{in}$ ,  $T_a$ , RH, WS and Pa, shown in the blue boxes of Fig. 3. With these inputs, this modeling framework simulated intermediate variables such as the SM proxy,  $f_{IPAR}$  and  $f_{APAR}$  and final variables, e.g. Rn, ET, GPP.

The first step for the instantaneous simulation was to estimate Rn, which is determined by  $SW_{in}$ , albedo ( $\alpha$ ),  $LW_{in}$  and  $LW_{out}$ , as shown in Eq. (12).  $SW_{in}$  in this study was obtained from the EC tower.  $\alpha$  was calculated based on the simple ratio vegetation index (SR) as Eqs. (13)–(14), which shows that albedo decreases as vegetation greenness increases (GAO, 1995). This method has been demonstrated to be an effective approach for various types of ecosystems (Mo et al., 2014).

$$Rn = (1 - \alpha)SW_{in} + LW_{in} + LW_{out} \quad (12)$$

$$\alpha = 0.28 - 0.14e^{(-6.08/SR^2)} \quad (13)$$

$$SR = (1+NDVI)/(1-NDVI) \quad (14)$$

$LW_{out}$  was estimated from UAS FLIR  $T_b$  by applying Stefan Boltzmann's law.  $LW_{in}$  for the instantaneous simulation was calculated by Stefan Boltzmann's law with atmospheric emissivity  $\epsilon_a$  as Eqs. (15)–(18) (Patra, 1996).

$$LW_{in} = \epsilon_a \sigma T_a^4 \quad (15)$$

$$\epsilon_a = 1 - (1 + \delta)e^{-\sqrt{(1.2+3\delta)}} \quad (16)$$

$$\delta = \frac{46.5}{T_a} e_0 \quad (17)$$

$$e_0 = RH \cdot 6.11e^{\left[\frac{L_v}{R_v} \left(\frac{1}{273.15} - \frac{1}{T_a}\right)\right]} \quad (18)$$

where  $e_0$  is the actual water vapor and was calculated based on the Clausius-Clapeyron equation.  $L_v = 2.5 \times 10^6$  (J kg<sup>-1</sup>) is the latent heat of vaporization and  $R_v = 461$  (J kg<sup>-1</sup>K<sup>-1</sup>) is the gas constant for water vapor.  $T_a$  is the air temperature (K).

The second step for the modeling framework (Fig. 3) was to estimate various environmental constraints from UAS NDVI and meteorological variables for the joint PT-JPL and LUE model, as shown in the Supplemental Table S1. Among them, the SM constraint was obtained from UAS thermal and optical observations. The SM proxy was calculated based on the temperature-vegetation triangle approach with theoretical dry and wet edges calculated from meteorological variables (Moran et al., 1994; Zhu et al., 2017). With this approach, the SM proxy could be used to indicate both spatial and temporal variations of SM. The details on using the temperature-vegetation triangle approach to estimate SM conditions can be found in Supplemental Section S2.

To obtain the actual land surface temperature ( $T_s$ ) from FLIR  $T_b$ , it is necessary to conduct the atmospheric correction to remove the longwave radiation reflected by the land surface and the upwelling longwave radiation to the sensor from the atmosphere. As shown in Eq. (19),  $\sigma T_b^4$  indicates the at-sensor thermal radiation recorded by FLIR.  $\epsilon_s \sigma T_s^4$  is the thermal radiation emitted from the surface.  $LW_{in}$  is the downwelling thermal radiation from the atmosphere to the land surface. The surface emissivity ( $\epsilon_s$ ) can be calculated based on the relation with NDVI as Eq. (20) (Van de Griend and M. Owe, 1993).  $LW_{atm}$  is the upwelling longwave radiation from the atmosphere to the sensor. Due to the low flight altitude and simplicity, this study neglected the influence of  $LW_{atm}$  as other UAS studies (e.g. Hoffmann et al., 2016; Ortega-Farías et al., 2016; Brenner et al., 2017).

$$\sigma T_b^4 = \epsilon_s \sigma T_s^4 + (1 - \epsilon_s)LW_{in} + LW_{atm} \quad (19)$$

$$\epsilon_s = \begin{cases} 0.986 & (NDVI > 0.608) \\ 1.0094 + 0.047 \ln(NDVI) & (0.131 < NDVI < 0.608) \\ 0.914 & (NDVI < 0.131) \end{cases} \quad (20)$$

where  $\sigma$  is the Stefan-Boltzmann constant ( $5.67 \times 10^{-8}$  W·m<sup>-2</sup>·K<sup>-4</sup>).  $T_s$

is the corrected land surface temperature (K).  $T_b$  is the brightness temperature from FLIR (K).  $LW_{in}$  is incoming longwave radiation (W·m<sup>-2</sup>).  $LW_{atm}$  is the upwelling longwave radiation (W·m<sup>-2</sup>) from the atmosphere to the sensor and is neglected in this study due to the low flight altitude.

Finally, with the simulated Rn and environmental constraints, the instantaneous simulation used the joint LUE and PT-JPL model to simulate ET, GPP, EF, LUE and WUE as shown in Fig. 3.

Based on the instantaneous simulation, this study also conducted the diurnal simulation to simulate the land surface fluxes for every half an hour during the flight campaign day to be complementary to the instantaneous simulation. With the observed Rn and meteorological variables from the EC tower, the diurnal simulation used spatially resolved information of vegetation and SM from UAS to simulate each half an hour during the course of the day. As the simulated VHR maps of fluxes can consider the variations of the EC footprints during the course of the day, the diurnal simulation can provide a precise way in validation of the temporal upscaling process from the instantaneous to the diurnal. Further, the EC footprints change positions with atmospheric conditions during the day. This offers opportunities for the EC technique to sample different areas around the tower to validate the obtained spatial patterns from UAS imagery. However, there are two assumptions for the diurnal simulation of this study. Vegetation and SM conditions are constant during the course of the day. Pixels in the simulated area have the same Rn as the observations from CNR4. For Rn, with a relatively homogeneous underlying surface on the EC flux site, all pixels are almost the same.

In the diurnal simulation, we further evaluated two schemes to scale up the instantaneous estimates of LE to the daytime averaged values. One scheme is to use EF obtained from the instantaneous simulation and assume EF remains constant during the daytime to calculate the averaged LE of daytime. Another scheme is by averaging all the instantaneous estimates of LE along the entire daytime period by considering the variations of the EC footprint with the aid of VHR imagery. Finally, the EC observations were used to compare the averaged daytime LE from these two schemes.

### 3.5. Model validation

This study validated intermediate and final variables (Fig. 3) in the modeling methodology. The observed fraction of intercepted PAR ( $f_{IPAR\_obs}$ ) as Eq. (21) was used to validate the simulated  $f_{IPAR}$  (equation in the supplemental Table S1). As shown in Eq. (2),  $f_{IPAR\_obs}$  was calculated based on measurements of the incident PAR above the canopy ( $PAR_{above}$ ), canopy-reflected PAR ( $PAR_{reflected}$ ) and the average of PAR below the canopy ( $PAR_{below}$ ) from eight understory sensors in Fig. 1.

$$f_{IPAR\_obs} = \frac{PAR_{above} - PAR_{reflected} - PAR_{below}}{PAR_{above}} \quad (21)$$

The simulated radiation components, e.g.  $SW_{net}$ ,  $LW_{in}$ ,  $LW_{out}$  (equivalent to  $T_b$  validation), and Rn were validated with measured radiation components within the FOV of CNR4 (Fig. 1). SM measurements from the campaign on 18th June 2017 were used to validate SM proxies estimated from the temperature-vegetation triangle approach. Details refer to Supplemental Section S2.

To validate the simulated final variables (e.g. LE, GPP, EF, LUE and WUE), the measured land surface fluxes from the EC tower were used. To compare with the simulated spatial land surface fluxes from UAS imagery, a footprint model, Flux Footprint Prediction (FFP), based on a scaling approach for the crosswind distribution of the flux footprint (Kljun et al., 2015) was used. At given EC site conditions and measurement height, the source area for a flux measurement varies with wind direction and atmospheric stability. This offers the opportunity to measure fluxes from different parts of the surface and to validate the spatial flux heterogeneity. The spatial source density distribution function can be described with 2D flux footprint functions that are

derived from atmospheric flow models (Metzger, 2018). In the flux simulation validation, the estimated source area density distribution was used together with a VHR resolution map of simulated fluxes to match the spatial resolutions between the UAS simulations and the EC fluxes and, hence, made them comparable. A threshold of 75% cumulated source contribution around the maximum of the footprint function was chosen to represent the source of EC measurements. Due to the long tails of the distribution function, the EC source area size increases dramatically beyond 75% of cumulated source area contribution (Kljun et al., 2015) whilst the source area density becomes very small.

For the EC system, due to the energy balance closure issue, the sum of measured sensible heat (H) and latent heat (LE) is often not equal to the available energy (net radiation minus ground heat flux,  $R_n - G$ ). To reduce the influence of the non-closure of energy balance, Energy balance Closure Ratio (ECR), as shown in Eq. (22), for each day was calculated and only measurements with  $EBR > 80\%$  were used for validation.

$$ECR = \frac{\sum (H + LE)}{\sum (R_n - G)} \quad (22)$$

Further, we also compared the simulated results with three different energy balance closure correction methods, which attributed the residual of the energy balance closure based on residual correction method (only to H or LE) and Bowen Ratio energy balance correction (Knauer et al., 2018).

1. Attribute all closure errors to H and keep LE as the uncorrected raw data (Larsen et al., 2016). LE\_EC1 was used to indicate the corrected LE from this method.
2. Attribute all closure errors to LE and keep H as the uncorrected raw data. LE\_EC2 was used to represent the corrected LE from this method.
3. Assuming that the ratio of sensible heat to LE (Bowen ratio) is correct, the residual of the energy balance is attributed to sensible and latent heat flux according to the Bowen ratio (Twine et al., 2000). LE\_EC\_BR was the corrected LE by this method.

$$LE\_EC1 = LE\_EC\_raw \quad (23)$$

$$LE\_EC2 = R_n - G - H\_EC\_raw \quad (24)$$

$$LE\_EC\_BR = \frac{R_n - G}{H\_EC\_raw + LE\_EC\_raw} LE\_EC\_raw \quad (25)$$

where  $LE\_EC\_raw$  is raw measurements of the latent heat flux ( $W \cdot m^{-2}$ ).  $H\_EC\_raw$  is raw measurements of the sensible heat flux ( $W \cdot m^{-2}$ ).  $R_n$  is the net radiation ( $W \cdot m^{-2}$ ).  $G$  is the ground heat flux ( $W \cdot m^{-2}$ ).

To validate the simulated land surface fluxes, statistics including root mean square deviation (RMSD), correlation coefficient (R) and relative errors (RE) were used.

$$RMSD = \sqrt{\sum_{i=1}^N (sim_i - obs_i)^2 / N} \quad (26)$$

$$R = \frac{\sum_{i=1}^N (sim_i - \overline{sim})(obs_i - \overline{obs})}{\sqrt{\sum_{i=1}^N (sim_i - \overline{sim})^2} \sqrt{\sum_{i=1}^N (obs_i - \overline{obs})^2}} \quad (27)$$

$$RE = (\overline{sim} - \overline{obs}) / \overline{obs} \quad (28)$$

where  $sim$  is the simulation.  $obs$  is the observation.  $i$  refers to the  $i$ th simulation or observation.  $N$  is the total number.  $\overline{sim}$  is the average of the simulation.  $\overline{obs}$  is the average of the observation.

### 3.6. Model error propagation analysis

To investigate the potential error propagation from the UAS imagery to the simulated land surface fluxes, e.g.  $R_n$ , SM, ET and GPP, an error propagation analysis was conducted. This analysis includes two

cases, the early growth stage with the atmospheric forcing on 25th May 2016, and a dense vegetation growth stage with the atmospheric forcing on 7th October 2016. For the early growth stage, the pixel was assumed to be NDVI equal to 0.35 with potential errors of  $\pm 0.1$  and  $T_b$  equal to  $27^\circ C$  with potential errors of  $\pm 2^\circ C$ . For the dense vegetation stage, the pixel was assumed to have NDVI equal to 0.82 with potential errors of  $\pm 0.1$  and  $T_b$  equal to  $10^\circ C$  with potential errors of  $\pm 2^\circ C$ . Simulations were run with varying levels of NDVI and  $T_b$  to simulate  $R_n$ , SM, ET and GPP. Then, the simulated  $R_n$ , SM, ET and GPP were compared with the simulated fluxes at the reference condition (NDVI = 0.35,  $T_b = 27^\circ C$  and NDVI = 0.82,  $T_b = 10^\circ C$ ) to estimate RE. This can help us to analyze the error propagation within the modeling methodology, further it can provide insights on the uncertainty of the simulated land surface fluxes respect to the uncertainties in UAS imagery.

### 3.7. Spatial heterogeneity analysis

One of the major benefits of UAS imagery is that VHR data can be used to detect spatial differences in the field, for instance, to further support spatial management in precision agriculture. Further, these VHR data can also help to identify the optimal spatial resolution (or the optimal UAS flying height) to capture significant differences in the landscape (Garrigues et al., 2006) and model benchmarking with EC (Kim et al., 2006). Semivariogram is an effective approach to assess the spatial structure of the heterogeneity (Curran, 1988). Therefore, this study used this approach to analyze the spatial structure of different variables including NDVI,  $T_s$ , and surface fluxes. The optimum resolution was identified to be half of the range of the semivariogram to capture differences between components in the landscape (Rahman et al., 2003). To avoid information from other landscapes (e.g. the nearby farm), the semivariogram analysis was only conducted for the willow plantation area, which is the source area for the EC measurements. The semivariograms of NDVI,  $T_b$ ,  $R_n$ , GPP, LE, EF, LUE and WUE for 25th May 2016 (early growth stage) and 07th Oct 2016 (dense vegetation stage) were analyzed to quantify the change of the spatial structure of the land surface fluxes.

A scaling experiment was conducted to assess the effects of aggregating UAS imagery pixels on the performance of the model benchmarking with EC observations. The purpose of this experiment was to establish the optimum spatial resolution for model validation and to have a confirmation of the validity of the spatial patterns of surface fluxes. Model inputs, NDVI and  $T_s$ , were aggregated to coarser spatial resolution and then these different spatial resolution data were used to simulated GPP and LE. Since this EC flux site is homogeneous, we selected the most heterogeneous UAS imagery collected on 25th May 2016 during the early growth period of vegetation for this experiment. The initial NDVI and  $T_s$  with a spatial resolution of 0.03 m were aggregated into 0.3, 1.5, 3, 6, 12, 24 m. These aggregated spatial resolution data were used as inputs of flux modeling and the simulated land surface fluxes were compared to EC observations.

To evaluate the influence of considering the heterogeneity of flux source contribution, we compared differences in model validation when using the arithmetic mean or the source weighted mean for pixels within the EC footprint. Calculating the arithmetic mean is equivalent to assuming that all pixels in the footprint contribute equally to fluxes measured by the EC tower, while the source weighted mean reflects that different parts of the footprint contribute differently to EC fluxes. Due to the particle dispersion process, the contribution from each pixel within the footprint is not spatially equal. This comparison provides insights into the importance of considering the source weighted EC footprint. Further, as we hypothesized in the introduction, if the simulated pattern is right, there should be an improvement for taking the source weighted contribution into consideration. Thus, this validation also provided the accuracy of the simulated spatial patterns to some extent.

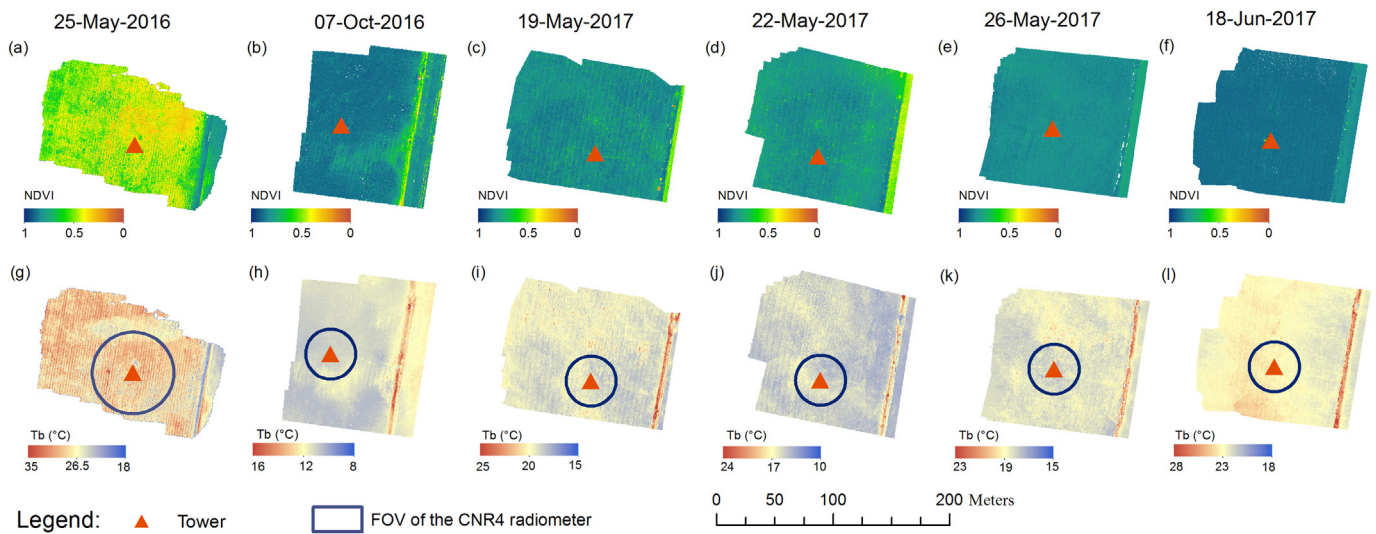


**Fig. 4.** Orthophotos of (a–f) NDVI and (g–l)  $T_b$ , (a, g) are on 25th May 2016. (b, h) are on 7th October 2016. (c, i) are on 19th May 2017. (d, j) are on 22nd May 2017. (e, k) are on 26th May 2017. (f, l) are on 18th June 2017. The NDVI for two flights on 2nd May 2016 and 12nd May 2016 are shown in Supplemental Fig. S5.

## 4. Results and discussion

### 4.1. Image validation

The produced orthophotos of NDVI and  $T_b$  from UAS images were shown in Fig. 4. The UAS flight campaigns of this study were conducted at a low altitude (12 m in the first three flights and 90 m in last five flights as shown in Table 1). UAS studies at such low flight altitude normally neglect the atmospheric correction, e.g. Hoffmann et al. (2016), Ortega-Farías et al. (2016) and Brenner et al. (2017). Our study only corrected the thermal data with the surface emissivity and the incoming longwave radiation, neglecting the effect of the atmospheric transmission from the surface to the sensor. To check the quality of these orthophotos for ET and GPP modeling, reflectance and  $T_b$  were validated with in-situ measurements as shown in Fig. 5.

Fig. 5 (a) indicates that there was a good accuracy for the reflectance at 670 and 800 nm with  $R^2 > 0.98$  and low RMSD about 3%. The reflectance from MCA is slightly lower than the reflectance from ASD on the ground (−1.11% and −1.48% for 800 nm and 670 nm, respectively). The radiance at the sensor tends lower than the reflected radiance at the surface could be due to the uncorrected atmospheric effects e.g. Rayleigh scattering, errors in the sensor radiometric calibration, or different FOVs of the validation sensor (ASD) and the MCA camera. However, this study used vegetation indices, which can further reduce the limited uncertainties in reflectance induced by the uncorrected atmospheric effects. For instance, Yu et al. (2016) assessed

the influence of atmospheric correction on UAS based NDVI at various flight altitudes (10, 30, 50, 100 m) and results indicate that the uncertainty in NDVI is only around 0.01. Therefore, this study did not conduct the atmospheric correction for the reflectance.

Fig. 5 (b) shows the comparison between UAS  $T_b$  and CNR4  $T_b$ . Results show that these two brightness temperatures were very close with  $R^2$  equal to 0.97 and RMSD about 0.93 °C. Errors of thermal data without the atmospheric correction may be significant for UAS, manned airborne and satellite platforms above 150 m (Berni et al., 2009; Hulley et al., 2012; Sabol et al., 2009). As shown in Eq. (19), the atmospheric correction of thermal data includes the correction of the reflected downwelling thermal radiation by accounting for the surface emissivity, and the correction of the atmospheric attenuation to exclude the upwelling thermal radiation from the atmosphere to the sensor. In this study, we conducted the correction of the downwelling thermal radiation by utilizing NDVI to calculate the surface emissivity. This correction approximately contributes to the improvement of the surface temperature about 1–2 °C. The MODTRAN (Berk et al., 1998) based typical atmospheric correction showed that the total errors for not correcting the atmospheric effects are around 2 °C at the 90 m flight altitude (Berni et al., 2009). It can be expected in this study without the correction of the atmospheric attenuation, the errors in the surface temperature can be around 1 °C and this also agrees with the comparison results between FLIR and CNR4. This 1 °C error can contribute to uncertainties in the longwave radiation budget to 10–15 W/m<sup>2</sup> based on the Stefan–Boltzmann law as Eq. (2). This accuracy fitted

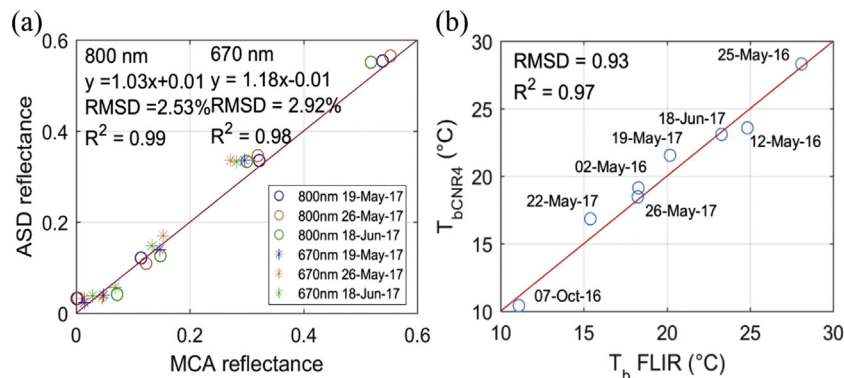


**Fig. 5.** Validation of UAS images. (a) Reflectance at 670 and 800 nm, (b) the comparison between FLIR  $T_b$  and CNR4  $T_b$ . The red line is the 1:1 line (Wang et al., 2018a). (For interpretation of the references to colour in this figure legend, the reader is referred to the web version of this article.)

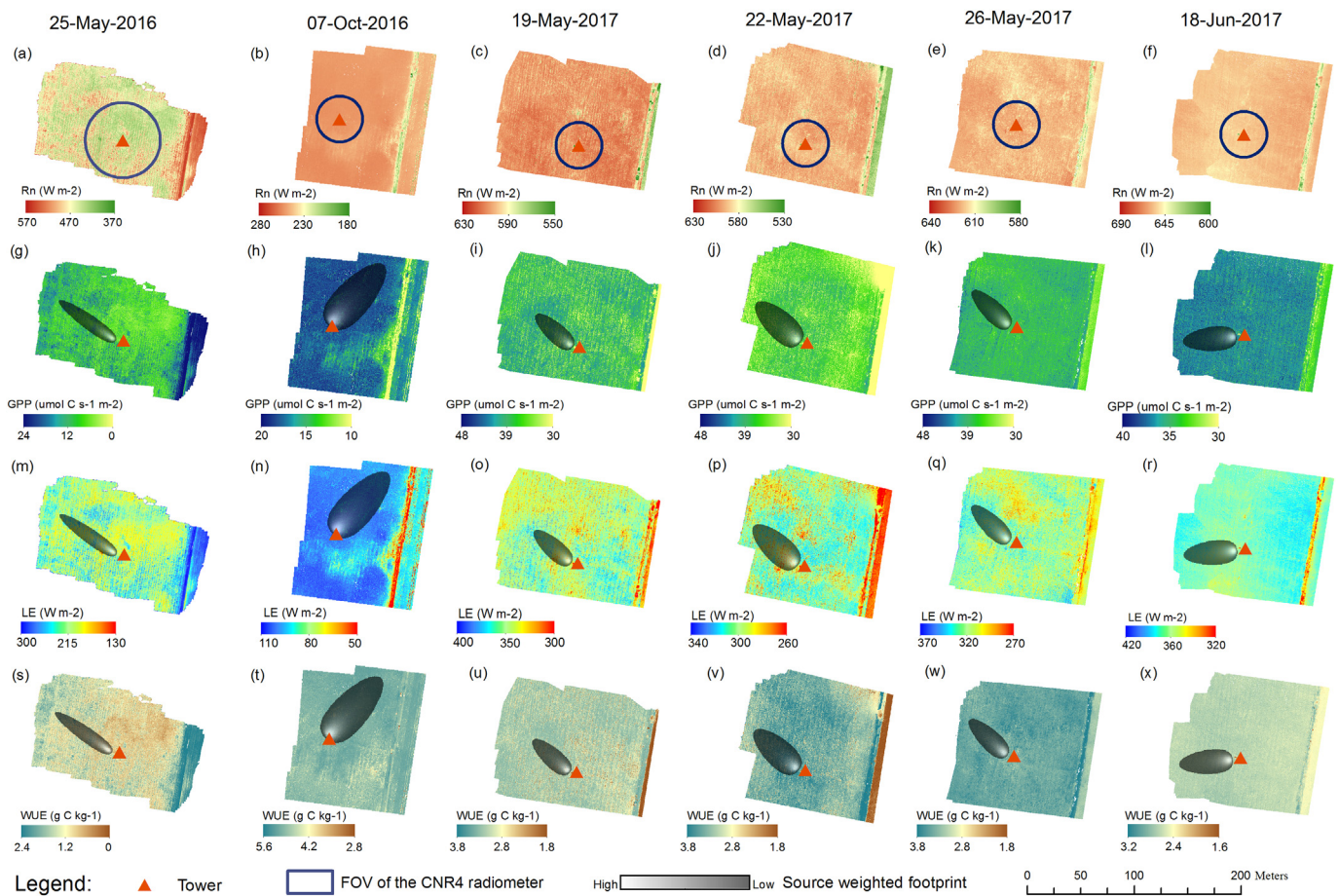


**Fig. 6.** Instantaneous simulation of (a–f) Rn, (g–l) GPP, (m–r) LE, and (s–x) WUE. The circles in (a–f) are the FOV of CNR4 with considering the change of vegetation height in Table 2. The shaded area in (g–x) indicates the source contribution of the EC footprint. Note the differences in the spatial resolutions and the dimensions of the displayed plots.

requirements for ET monitoring with an accuracy of 10% in ecosystem and crop management (Fisher et al., 2017).

Besides the atmospheric correction, this study did not consider the normalization of reflectance and thermal data between the flight trajectory due to the short flight duration time (approximately 10 min, Table 1). Additionally, the anisotropy effects of thermal and optical data may also contribute to uncertainties. In general, these issues can contribute to the uncertainties of UAS data and further to the simulated fluxes. However, the validation of our study (Fig. 5) shows UAS imagery has acceptable accuracy.

#### 4.2. Instantaneous simulation

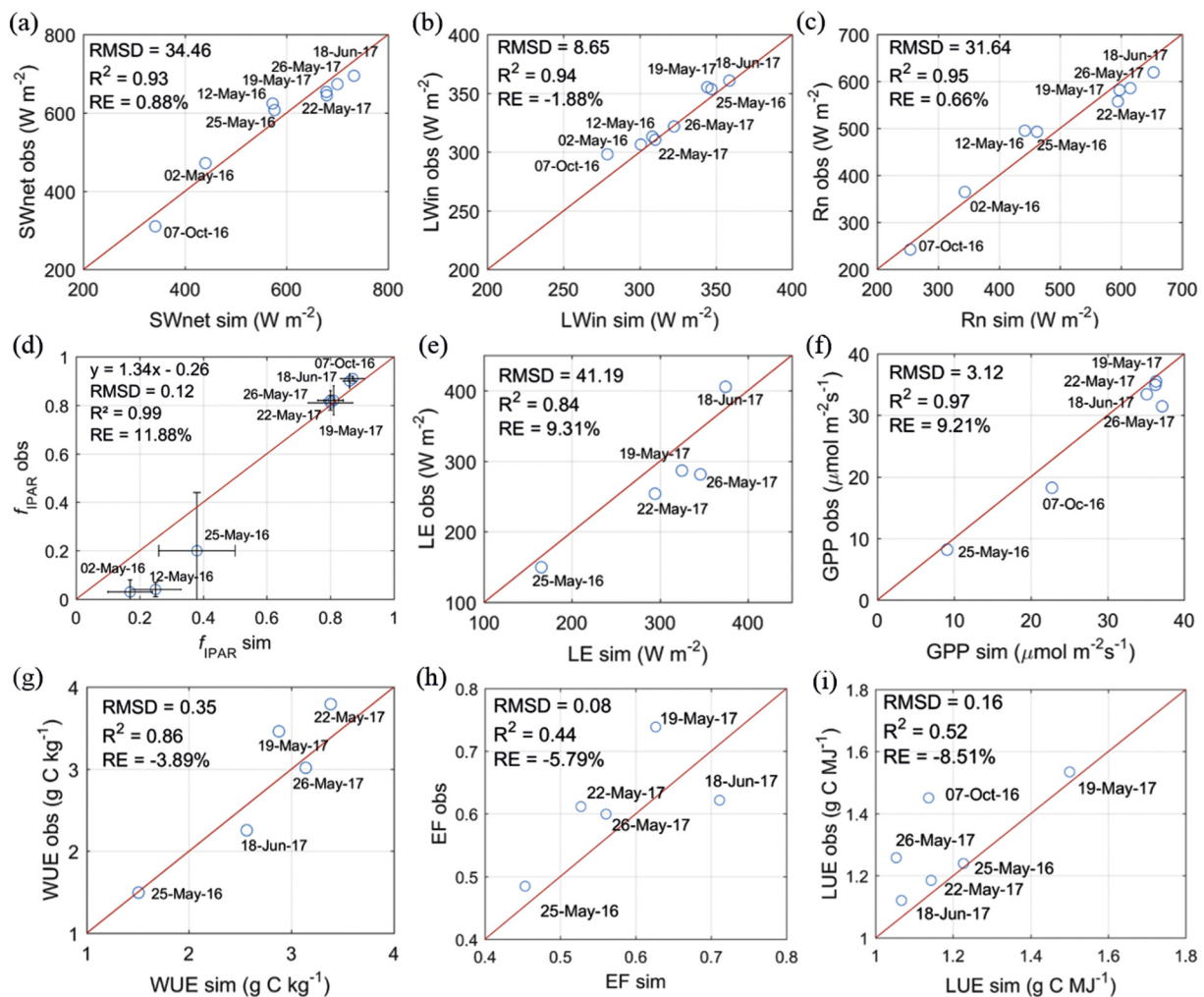
The spatial patterns of simulated final variables Rn, GPP, LE and WUE are shown in Fig. 6. Compared to the NDVI pattern, it can be seen that in the dense vegetation area (high NDVI), Rn was higher than the areas with less dense vegetation. GPP followed the spatial pattern of NDVI. With higher NDVI, there was a higher GPP. For LE, during the early growth stage (25th May 2016), it followed the pattern of the SM proxy, while during the dense vegetation periods (other flights), it had the similar pattern as Rn. For WUE, the pattern was a combination of GPP and LE but more similar to GPP.

Fig. 7 (a–c) shows validation of the simulated  $SW_{net}$ ,  $LW_{in}$  and Rn with considering the FOV of CNR4 (Fig. 6 a–f). This modeling methodology can well simulate  $SW_{net}$ ,  $LW_{in}$  and Rn with RMSDs of 34.46, 8.65 and 31.64  $W\cdot m^{-2}$ , respectively.  $R^2$  between the observed and the simulated  $SW_{net}$ ,  $LW_{in}$  and Rn were 0.93, 0.94 and 0.95, respectively. The relative errors (RE) for  $SW_{net}$ ,  $LW_{in}$  and Rn were 0.88%, –1.88%

and 0.66%, respectively. As shown in Fig. 7 (d), the model could simulate  $f_{IPAR}$  with RMSD equal to 0.12. The simulated spatial patterns and validation results on the estimated SM proxy were shown in Supplemental Figs. S2 and S3.  $R^2$  between in-situ and the estimates SM for temporal variations and spatial variations reached to 0.77 and 0.50, respectively.

Considering the source weighted EC footprint (the shaded area in Fig. 6), the model simulated the dynamic of LE, GPP, and WUE with RMSDs of 41.19  $W\cdot m^{-2}$ , 3.12  $\mu mol\cdot C\cdot m^{-2}\cdot s^{-1}$ , and 0.35  $g\cdot C\cdot kg^{-1}$ , respectively, as shown in Fig. 7 (e–g).  $R^2$  for these simulations are 0.84, 0.97, and 0.86, respectively. RE for the simulated LE, GPP, and WUE are 9.31%, 9.21%, and –3.89%, respectively. Compared to other studies using UAS data to simulate LE, this study has a similar or even better performance (Brenner et al., 2017; Hoffmann et al., 2016; Ortega-Farías et al., 2016). This could be partially due to that this site is the radiation controlled system (Wang et al., 2018b) and this methodology can give a good estimation of Rn as Fig. 7 (c).

To normalize the estimated ET and GPP with Rn and APAR, we calculated EF and LUE respectively, as Fig. 7 (h and i). Results show that this model achieved a moderate simulation performance with the RMSDs of EF and LUE equal to 0.08 and 0.16  $g\cdot C\cdot MJ^{-1}$ , respectively.  $R^2$  for these simulations are 0.44 and 0.52, respectively. RE for the simulated EF and LUE are –5.79% and –8.51%, respectively. The possible approach for future improvement of this modeling methodology is to introduce more spectral indices to better characterize the vegetation physiological status to constrain LUE and EF. For instance, the photochemical reflectance index (PRI) (Gamon et al., 1992) can be utilized to indicate the light use efficiency to constrain the estimation of GPP and



**Fig. 7.** Comparison of simulated land surface fluxes from UAS instantaneous simulations with in-situ measurements. (a)  $SW_{net}$ , (b)  $LW_{in}$ , (c)  $R_n$ , (d)  $f_{IPAR}$ , (e) GPP, (f) LE, (g) WUE, (h) EF, (i) LUE. The error bars in (d) indicate the standard deviations of the observed and estimated  $f_{IPAR}$  in the EC footprint. It should be noticed that energy relative balance closure of the measurements on 7th October 2016 was lower than 80% and this date was excluded in LE, WUE and EF analysis. The red line is the 1:1 line. (For interpretation of the references to colour in this figure legend, the reader is referred to the web version of this article.)

transpiration. However, it should be noted that in the short time scales, PRI reflects the xanthophyll de-epoxidation and can indicate the change of LUE (Zarco-Tejada et al., 2013a). In the seasonal scales, the change of PRI is more complex. The changes are related to the size of constitutive pigment pools (Zhang et al., 2016) as well as affected by structural changes (Zhang et al., 2017) over the seasons. Additionally, the green or the red edge based vegetation indices can also be utilized to improve the estimation of the green vegetation fraction (Gitelson et al., 2003; Viña et al., 2011). In current methodology, only the soil adjusted vegetation index (SAVI) (Huete, 1988) with the empirical formula from the PT-JPL model (Fisher et al., 2008) was utilized to estimate the green vegetation fraction.

#### 4.3. Diurnal simulation

The simulated spatial patterns of the diurnal LE simulation for the half an hour of flight campaigns are shown as the base map in Fig. 8. Compared to the simulated instantaneous LE at the same time in Fig. 6 (k–o), the simulated spatial patterns were similar and the estimated values were close. Fig. 9 shows ECR and the comparison between the simulated LE and GPP with EC observations for each day. Generally, the diurnal simulation captured the observed diurnal variations of LE and GPP. In most cases, the simulated LE was within the LE with residual closure, as shown in Fig. 9 (a–e). The model was also able to estimate

GPP, as shown in Fig. 9 (f–j). But during the noon period, the simulation slightly overestimated GPP, while during other hours the simulation underestimated GPP. The reason may be that the GPP model of this study did not consider the influence of the PAR intensity to LUE. During the mid-day, the high PAR intensity can induce the saturation of the canopy photosynthesis and reduce canopy LUE (Ibrom et al., 2008; Propastin et al., 2012).

Table 3 presents the statistics on the model validation and the simulated LE was compared with different energy balance closure correction methods. Fig. 10 (a) and (b) shows the scatterplots between the simulated and the observed GPP and LE fluxes in the diurnal simulation. Because ECR on 7th October 2016 was lower than 80%, the simulation of LE on this day was excluded in the analysis. Compared to other energy balance closure correction methods (LE\_EC\_1 and LE\_EC\_2), LE\_EC\_BR shows the best match with the simulated LE.  $R^2$  and RE for the simulated LE were  $39.33 \text{ W m}^{-2}$ , 0.87 and 0.52%, respectively. The diurnal simulation could well capture GPP dynamics with RMSD of  $5.04 \mu\text{mol C m}^{-2} \text{ s}^{-1}$ ,  $R^2$  of 0.83 and RE of  $-7.58\%$ . As the variations of EC footprints sample different source areas around the tower during the course of the day, the good performance of the diurnal simulation gives confidence for the simulated spatial patterns from UAS imagery. It should be also noted that the diurnal simulation of this study has assumptions that NDVI and SM are constant during the course of the day. For NDVI, it is a reasonable assumption. Regarding SM, the

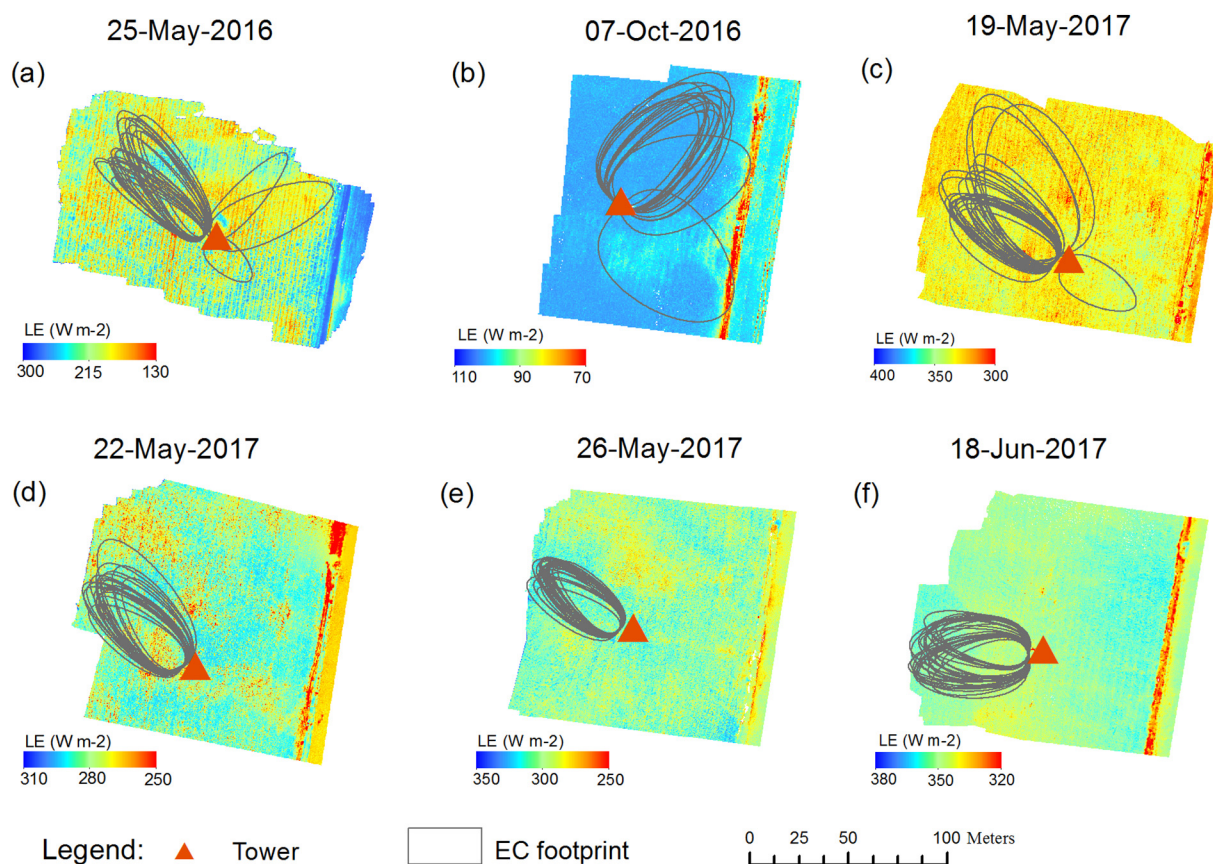


Fig. 8. Simulated spatial patterns of the diurnal LE simulation at half an hour when UAS campaigns were conducted. The EC footprints show the coverage of the footprint for each half an hour during the daytime of the UAS flight campaign day. In the validation, the source weighted footprints were used.

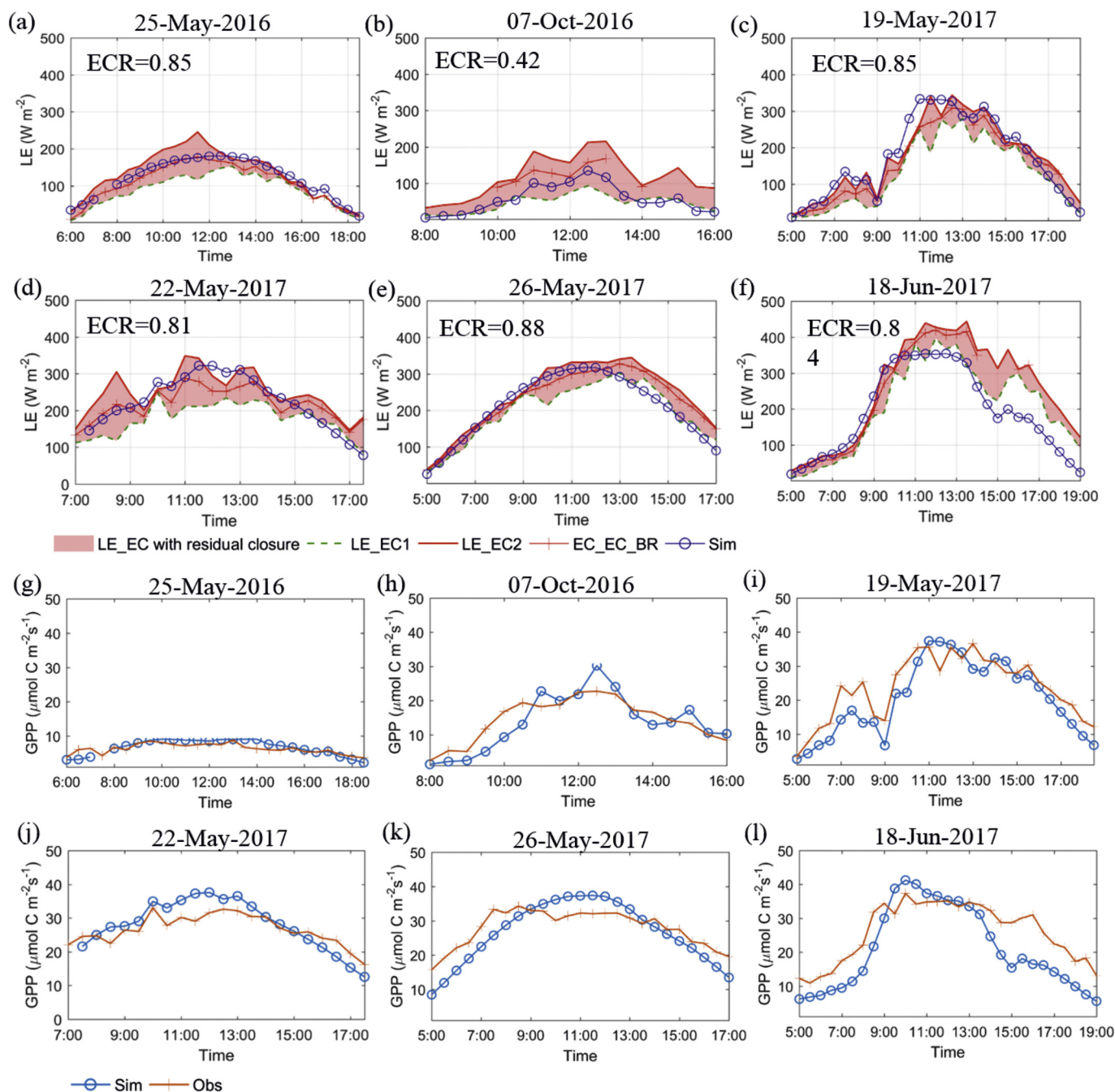
in-situ measurements in our site show that it is almost constant within one day as the Supplemental Fig. S4. However, in dry regions, the variations of the soil moisture during the course of a day may need to take into account. Further studies as (Malbêteau et al., 2018) to conduct several flights during the course of the day to explore the diurnal variations of the land surface energy components and fluxes are needed.

Fig. 10 (c) shows the comparison of these two temporal upscaling schemes, averaging from the instantaneous simulations considering the variations of the EC footprint and assuming a constant daily EF during the course of the day. It can be seen that compared to EC observations, the averaged daytime LE from all instantaneous simulations by considering the variations of the EC footprint has  $R^2$  of 0.92, while the averaged LE by using a constant daily EF has  $R^2$  of 0.89. Similarly, the scheme with averaged LE from all instantaneous simulations has a lower RMSD than the scheme using a constant daily EF. To normalize the averaged daytime LE with  $R_n$ , we found more difference between these two schemes. Compared to EC observations, the EF from the scheme of averaged LE from instantaneous simulations has  $R^2$  of 0.64, while the EF for the scheme with a constant daily EF is equal to 0.57. These findings agree with Morillas et al. (2014) that averaging the instantaneous estimates performs better than assuming the self-preservation of EF for the temporal upscaling from the instantaneous to the diurnal. Moreover, this indicates the importance to consider the variations of the EC footprint during the course of a day in model benchmarking.

#### 4.4. Model error propagation

Fig. 11 shows the results of error propagation from UAS imagery to the simulated  $R_n$ , SM, ET and GPP. The NDVI and  $T_b$  determine the surface albedo and  $LW_{out}$ , respectively. Their uncertainties influence

the estimated  $R_n$  of the land surface. Thus, it can be seen that with  $\pm 0.1$  errors in NDVI and  $\pm 2^\circ\text{C}$  errors in  $T_b$ , the simulated  $R_n$  changed approximately  $\pm 6\%$  in both the early growth and dense vegetation stages. For SM which was estimated from the temperature-vegetation triangle approach, the possible errors of NDVI and  $T_b$  can alter the relative position of the pixel respected to the dry and wet edges within the triangle and change the estimated SM. As shown in Fig. 11, the estimated SM has different responses to the errors in NDVI and  $T_b$  in the early growth stage and dense vegetation stage. In the early growth stage, these errors of UAS imagery only contributed to changes of SM within 5%. However, in the dense vegetation growth stage, the errors lead to the SM changes up to 60%. This is due to that in the dense vegetation conditions (high vegetation fraction), the dry and wet edges of the triangle approach have a closer distance than in the low vegetation fraction (Garcia et al., 2014). Further for the estimation of ET, with  $\pm 6\%$  errors from  $R_n$  and  $\pm 5\%$  errors from SM, the error propagation led to  $\pm 12\%$  uncertainties in LE for the early growth stage. However, for the dense vegetation growth stage, with the  $\pm 6\%$  errors from  $R_n$  and  $\pm 60\%$  errors from SM, the simulated LE has lower uncertainties within 30%. This is due to that for the dense vegetation conditions, the methodology of this study is more similar to the vegetation driven approach, which is the Priestley-Taylor approach to estimate ET and less relies on the accuracy of surface temperature and SM (McCabe et al., 2017). Thus, it can reduce the uncertainties from the estimated SM. For the bare soil conditions, more radiation is partitioned to the soil surface and this methodology is more close to the Temperature-Vegetation triangle approach for the estimation of LE. Therefore, in this way this methodology can achieve a good accuracy to estimate ET for both early growth and dense vegetation conditions. In the error propagation of GPP, for the low vegetation conditions, GPP is more sensitive to the variation of NDVI and  $\pm 0.1$  errors in NDVI can



**Fig. 9.** Simulated diurnal variation of (a–f) LE and (g–l) GPP. LE\_EC1 was attributing all closure errors to the sensible heat flux. LE\_EC2 was attributing all closure errors to the latent heat flux. LE\_EC\_BR was attributing closure errors to both latent heat flux and sensible heat flux with keeping the fixed Bowen ratio. The ECR of each day is shown in each plot. Note that ECR on 7th October 2016 was < 0.80.

**Table 3**

Statistics for validation of the diurnal simulation (LE was compared with different energy balance closure correction methods).

	RMSD	R <sup>2</sup>	RE (%)
LE_EC1 (W·m <sup>-2</sup> )	48.65	0.84	17.89
LE_EC2 (W·m <sup>-2</sup> )	44.58	0.86	-8.35
LE_EC_BR (W·m <sup>-2</sup> )	39.37	0.85	0.80
GPP (μmol·C·m <sup>-2</sup> ·s <sup>-1</sup> )	5.04	0.83	-7.58

contribute to 40% changes of GPP. However, in the dense vegetation conditions, NDVI gets saturation and the simulated GPP does not change so much.

#### 4.5. Spatial heterogeneity

Fig. 12 shows the comparison of the semivariograms on different growth stages. It can be seen that the sill values (semivariance when the semivariogram flattens out, the y-axis value) of all variables except SM during the early growth stage (25th May 2016) were larger than that during the dense vegetation period (07th Oct 2016). Furthermore, from the range (the lag distance when the sill is reached, the x-axis value), it can also be found that the range on 25th May 2016 is much smaller than 07th Oct 2016. These findings indicate the landscape was more heterogeneous on the early growth stage than the dense vegetation stage. During the early growth stage, the values of the range were around 1.5–2 m. This range is approximately equal to the canopy crown

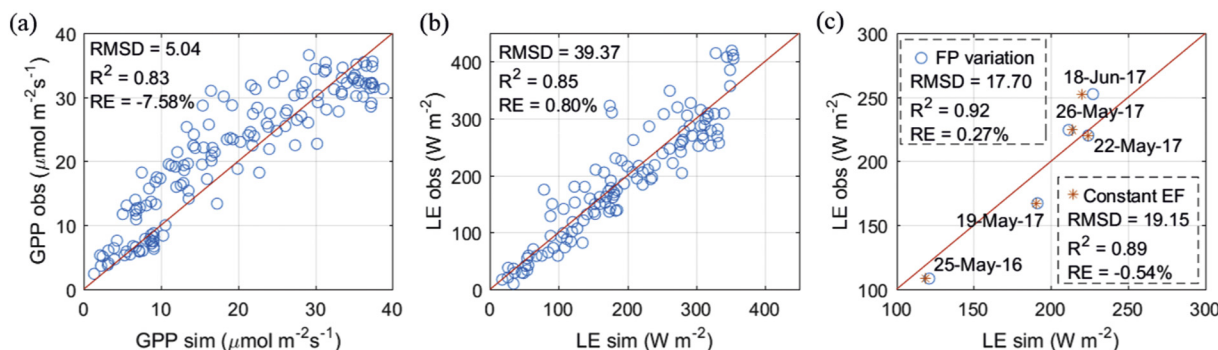


**Fig. 10.** Scatter plots between the simulated and the observed (a) GPP and (b) LE. Source weighted EC footprints were used in the validation. (c) is the comparison between two temporal upscaling schemes from the instantaneous to the daytime average. The blue circle uses the averaged LE from all instantaneous simulations with considering the variations of EC footprint (FP) to sample different areas around the EC tower. The red star represents using a constant evaporative fraction from the instantaneous to the daytime average. ECR on 7th October 2016 was < 0.80 and LE of this day was excluded in the analysis. (For interpretation of the references to colour in this figure legend, the reader is referred to the web version of this article.)

size and the open-canopy structure at the early stage contributes the spatial covariance within this range. For this early growth stage, to capture the variability, an optimum pixel size would be half of the range (Rahman et al., 2003) around 1 m. However, when the willow plantation grew to the closed canopy structure, the range values for the semivariograms were much larger. By comparing the nugget (the semivariance value when the lag is equal to 0 m) and range values, it can be found that the spatial structure of GPP, LUE and WUE resembled that of NDVI, while the spatial structure of the Rn, SM, LE and EF were similar to those of  $T_b$ . These findings agree with previous findings that in the radiation controlled Danish ecosystem, vegetation greenness controls the carbon assimilation, while the net radiation controls LE and WUE is mainly determined by GPP (Wang et al., 2018b).

For the scaling experiment, the relationship between the accuracy of simulation outputs and degradation of the spatial resolution of inputs is shown in Fig. 13. We found that the model performance did not change significantly when the spatial resolution was degraded from 0.03 to 1.5 m. There is slightly performance degradation from 1.5 to 12 m, but there was a clear loss in model accuracy when the spatial resolution was degraded from 12 to 24 m. The better result of using finer spatial resolution data agrees with other scaling experiments with satellite data (Ershadi et al., 2013). It also indicates the accurate simulation patterns that our UAS based methodology captured. However, this study also found no significant improvements with using super high spatial

resolution data (between 0.03 and 1.5 m) at this site. This indicates that comparing to the observations at the EC flux tower, too high spatial resolution remote sensing data may not be necessary.

As the comparison between the solid and dashed lines in Fig. 13, the model validation using a source weighted footprint, which considered the heterogeneity of EC source contribution within the footprint, showed a significantly better performance than using arithmetic mean. In the case of GPP,  $R^2$  was around 10% higher and RMSD 30% lower when using the source weighted footprint until reaching a resolution of 12 m. It was noticed also a slight decrease in  $R^2$  at the 1.5 m pixel size, which corresponded with the range of the semivariogram for GPP and LE. These results indicate the importance to consider the heterogeneity of the EC source contribution, especially during the early growth stage of vegetation. Furthermore, these results also provide confidence in the spatial pattern of fluxes, as we hypothesized that if the spatial patterns were not accurate, we would not see an improvement in model performance using the weight contribution to the total flux. These results also suggest that in our conditions and for model validation purposes, it is enough to have a spatial resolution of around 12 m (flight height of 4 km) and for detecting spatial differences a spatial resolution of 1 m (half of the semivariogram range) (flight height of 400 m) should be enough at this site. This demonstrates an approach relying on the analysis of spatial heterogeneity of high spatial resolution UAS data to determine the optimum flying height (spatial resolution). The optimal

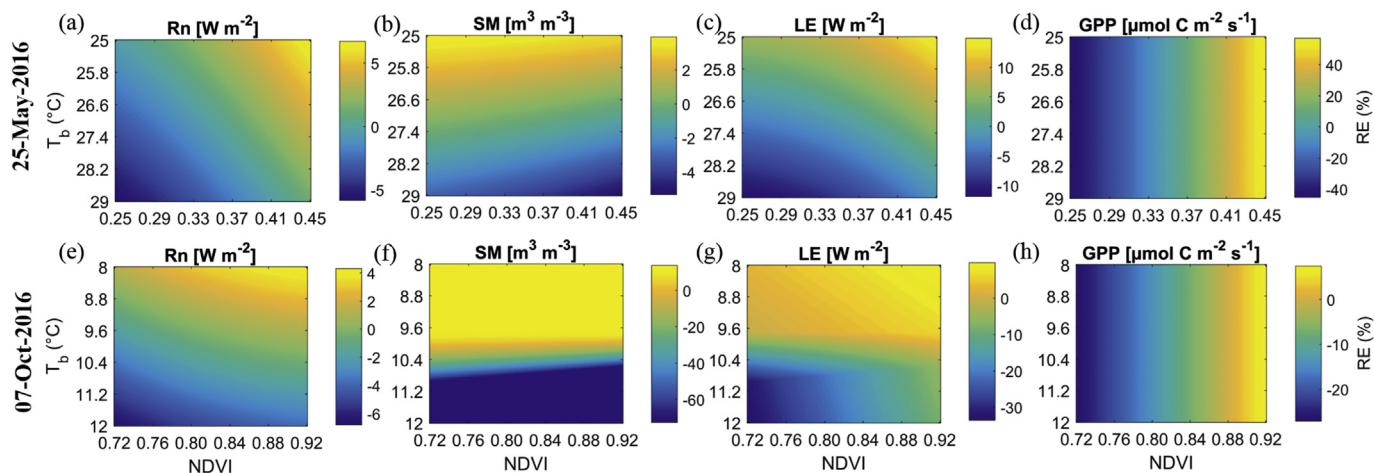


**Fig. 11.** Error propagation analysis from uncertainties of UAS imagery to the simulated fluxes. The first panel (a–d) is for the early growth stage with NDVI of 0.35 and  $T_b$  of 27 °C and the atmospheric forcing on 25th May 2016. The second panel (e–h) is for the dense vegetation growth stage with NDVI of 0.82 and  $T_b$  of 10 °C and the atmospheric forcing on 7th Oct 2016. Simulations were conducted with adding errors of NDVI equal to  $\pm 0.1$  and errors of  $T_b$  equal to  $\pm 2$  °C. (a) and (e) are the errors of simulated Rn. (b) and (f) are the errors for the simulated SM. (c) and (g) are the errors for the simulated LE. (d) and (h) are the errors for the simulated GPP.

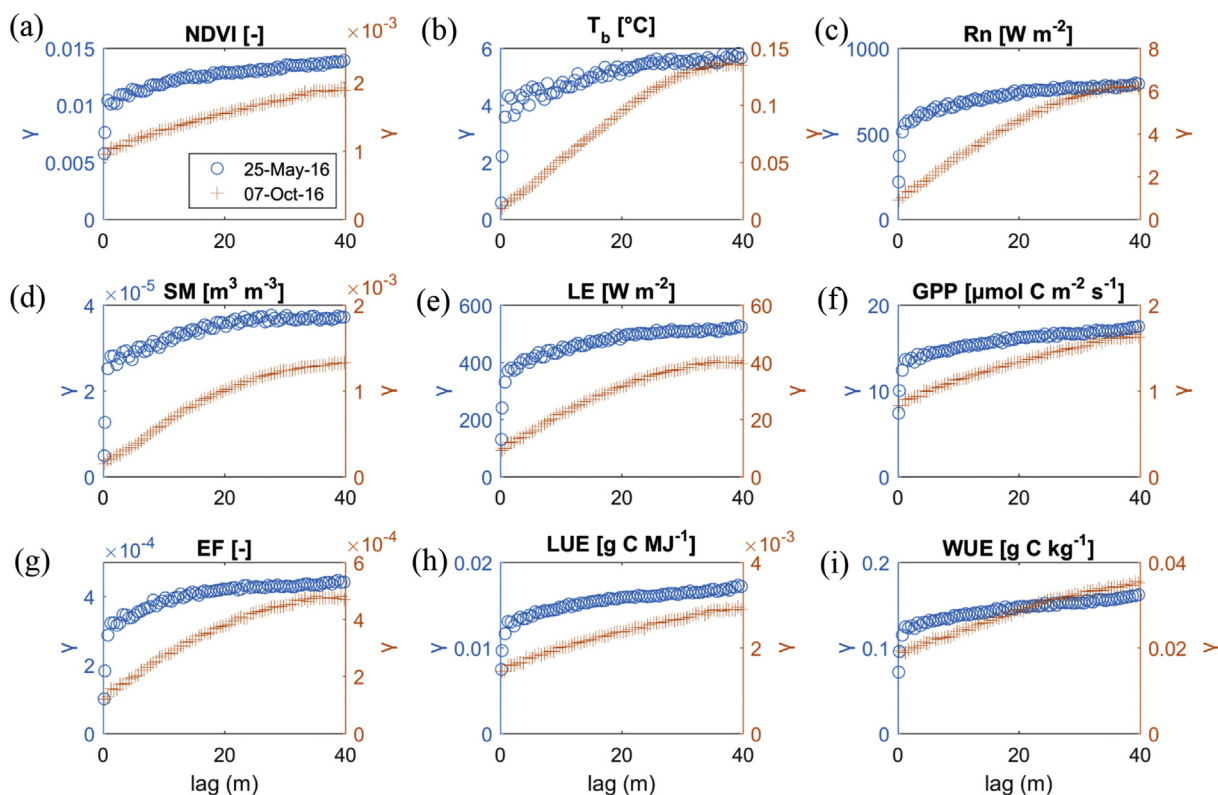


**Fig. 12.** Semivariograms of (a) NDVI, (b)  $T_b$ , (c) SM, (d) Rn, (e) GPP, (f) ET, (g) WUE, (h) EF and (i) LUE on 25th May 2016 (the early growth stage, blue circles) and 07th Oct 2017 (the dense vegetation stage, orange dots). The y-axis  $\gamma$  is the semivariance. The left y-axis is 25th May 2016 and the right y-axis is 07th Oct 2016. (For interpretation of the references to colour in this figure legend, the reader is referred to the web version of this article.)

resolution is the one that captures sufficient spatially resolved information while maximizing the ground coverage and will change depending on each specific site conditions. A targeted spatial scale analysis using the semivariogram and aggregation experiments as this study can be applied in other sites to identify such optimal spatial resolution and optimal flight height for UAS.

### 5. Conclusions

This study designed and evaluated an operational monitoring methodology of mapping land surface energy, water and CO<sub>2</sub> fluxes specifically for unmanned aerial systems (UAS). It integrates optical and thermal imagery to map the land surface fluxes at an optimal spatial resolution to maximize the ground coverage of the area while having sufficient spatial details to capture fluxes accurately. This

methodology is based on a joint parsimonious evapotranspiration (ET) and gross primary productivity (GPP) model with limited data inputs and parameterization and could even be applied in data-scarce regions. We showed that it can provide very high resolution (< 1 m) maps of land surface fluxes such as net radiation (Rn), ET, GPP, evaporative fraction (EF), light use efficiency (LUE) and ecosystem water use efficiency (WUE).

The study was carried out at a flux site deciduous willow plantation where EC data are available for model validation. Our model validation results for the instantaneous Rn, ET, GPP, EF, LUE and WUE showed root-mean-square deviations equal to 31.6 W·m<sup>-2</sup>, 41.2 W·m<sup>-2</sup>, 3.12 μmol·C·m<sup>-2</sup>·s<sup>-1</sup>, 0.08, 0.16 g·C·MJ<sup>-1</sup> and 0.35 g·C·kg<sup>-1</sup>, respectively. Further, in the temporal upscaling from the instantaneous to the diurnal, it was found that averaging the instantaneous simulations performs better than the classic approach of assuming a constant

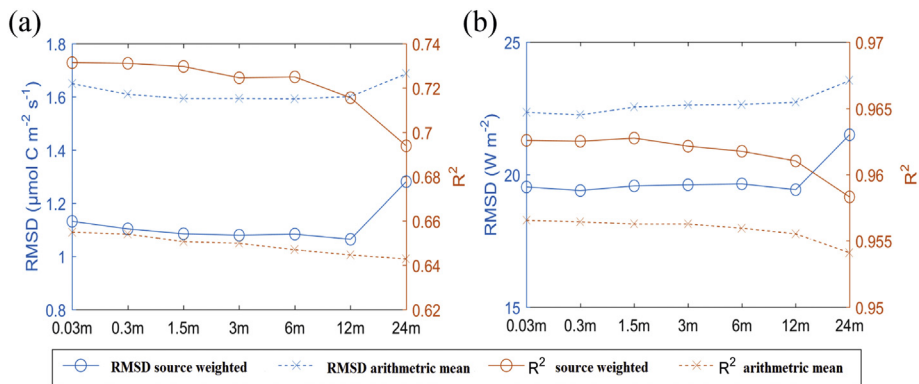


**Fig. 13.** Comparison of model simulation performance (a: GPP, b: LE) with the EC observations across aggregated spatial resolutions from 0.03 to 24 m and the performance using the source weighted mean (curves with circles) and arithmetic mean (curves with cross signs) of EC footprints.

evaporative fraction. Using a footprint model to sample different areas of high spatial resolution UAS imagery can be a tool to upscale to diurnal estimates to benchmark with EC data.

Moreover, we showed how spatial metrics derived from high-resolution maps can be used to identify the optimum spatial resolution to capture the ET and GPP fluxes accurately. We found that a resolution consistent with the canopy size (around 1.5 m in our study) is sufficient to capture the spatial heterogeneity of the fluxes. Compared to the EC observations, in this willow site, the aggregation of simulated GPP using source weighted mean of the footprint was about 10% higher in  $R^2$  and the RMSD was 30% lower than using the arithmetic mean, during an early growth stage. This improvement highlights the need for considering the heterogeneity of the land surface and flux source contribution within the eddy covariance footprint, especially during the early growth stage. Further, the improvement also indicates the accuracy of the obtained spatial patterns, since if the spatial patterns would be incorrect, such an improvement would not be expected.

This methodology has a large potential to provide spatially resolved information on ecohydrological processes valuable for agricultural and natural ecosystems applications. The unprecedentedly high spatial resolution obtained is useful to examine scaling issues, benchmark models with eddy covariance fluxes and quantify spatial heterogeneity within biomes.

## Acknowledgement

The authors would like to thank the European Union (EU) and Innovation Fund Denmark (IFD) for funding, in the frame of the collaborative international consortium AgWIT financed under the ERA-NET Co-fund Water Works 2015 Call. This ERA-NET is an integral part of the 2016 Joint Activities developed by the Water Challenges for a Changing World Joint Programme Initiative (Water JPI). This study was also supported by the Smart UAV project from IFD [125-2013-5]. SW was financed by an internal PhD grant from the Department of Environmental Engineering at DTU and SW conducted a short term research stage with PZT through the COST action OPTIMISE. The authors would like to thank the editors and three anonymous reviewers for the comments and suggestions to improve the quality of this paper.

## Appendix A. Supplementary data

Supplementary data associated with this article can be found in the online version, at <https://doi.org/10.1016/j.rse.2019.03.040>. These data include the Google map of the most important areas described in this article.

## References

- Amthor, J.S., Chen, J.M., Clein, J.S., Frolking, S.E., Goulden, M.L., Grant, R.F., Kimball, J.S., King, A.W., McGuire, A.D., Nikolov, N.T., Potter, C.S., Wang, S., Wofsy, S.C., 2001. Boreal forest CO<sub>2</sub> exchange and evapotranspiration predicted by nine ecosystem process models: intermodel comparisons and relationships to field measurements. *J. Geophys. Res. Atmos.* <https://doi.org/10.1029/2000JD900850>.
- Anderson, K., Gaston, K.J., 2013. Lightweight unmanned aerial vehicles will revolutionize spatial ecology. *Front. Ecol. Environ.* 11, 138–146. <https://doi.org/10.1890/101890.120150>.
- Baldocchi, D.D., 2003. Assessing the eddy covariance technique for evaluating carbon dioxide exchange rates of ecosystems: past, present and future. *Glob. Chang. Biol.* 9, 479–492. <https://doi.org/10.1046/j.1365-2486.2003.00629.x>.
- Bandini, F., Lopez-Tamayo, A., Merediz-Alonso, G., Olesen, D., Jakobsen, J., Wang, S., Garcia, M., Bauer-Gottwein, P., 2018. Unmanned aerial vehicle observations of water surface elevation and bathymetry in the cenotes and lagoons of the Yucatan Peninsula, Mexico. *Hydrogeol. J.* 1–16.
- Beer, C., Reichstein, M., Tomelleri, E., Ciais, P., Jung, M., Carvalhais, N., Rödenbeck, C., Arain, M.A., Baldocchi, D., Bonan, G.B., Bondeau, A., Cescatti, A., Lasslop, G., Lindroth, A., Lomas, M., Luyssaert, S., Margolis, H., Oleson, K.W., Rouspard, O., Veenendaal, E., Viovy, N., Williams, C., Woodward, F.I., Papale, D., 2010. Terrestrial gross carbon dioxide uptake: global distribution and covariation with climate. *Science (80-)* 329, 834–838. <https://doi.org/10.1126/science.1184984>.
- Berk, A., Bernstein, L.S., Anderson, G.P., Acharya, P.K., Robertson, D.C., Chetwynd, J.H., Adler-Golden, S.M., 1998. MODTRAN cloud and multiple scattering upgrades with application to AVIRIS. *Remote Sens. Environ.* 65, 367–375. [https://doi.org/10.1016/S0034-4257\(98\)00045-5](https://doi.org/10.1016/S0034-4257(98)00045-5).
- Berni, J., Zarco-Tejada, P.J., Suarez, L., Fereres, E., 2009. Thermal and narrowband multispectral remote sensing for vegetation monitoring from an unmanned aerial vehicle. *IEEE Trans. Geosci. Remote Sens.* 47, 722–738. <https://doi.org/10.1109/TGRS.2008.2010457>.
- Brenner, C., Thiem, C.E., Wizemann, H.D., Bernhardt, M., Schulz, K., 2017. Estimating spatially distributed turbulent heat fluxes from high-resolution thermal imagery acquired with a UAV system. *Int. J. Remote Sens.* 38, 3003–3026. <https://doi.org/10.1080/01431161.2017.1280202>.
- Brutsaert, W., Sugita, M., 1992. Application of self-preservation in the diurnal evolution of the surface energy budget to determine daily evaporation. *J. Geophys. Res.* <https://doi.org/10.1029/92JD00255>.
- Chen, J., Liu, J., Cihlar, J., Goulden, M., 1999. Daily canopy photosynthesis model through temporal and spatial scaling for remote sensing applications. *Ecol. Model.* [https://doi.org/10.1016/S0304-3800\(99\)00156-8](https://doi.org/10.1016/S0304-3800(99)00156-8).
- Colaizzi, P.D., Evett, S.R., Howell, T.A., Tolk, J.A., 2006. Comparison of five models to scale daily evapotranspiration from one-time-of-day measurements. *Trans. ASABE.* <https://doi.org/10.13031/2013.22056>.
- Curran, P.J., 1988. The semivariogram in remote sensing: an introduction. *Remote Sens. Environ.* 24, 493–507. [https://doi.org/10.1016/0034-4257\(88\)90021-1](https://doi.org/10.1016/0034-4257(88)90021-1).
- Damm, A., Paul-Limoges, E., Haghghi, E., Simmer, C., Morsdorf, F., Schneider, F.D., van der Tol, C., Migliavacca, M., Rascher, U., 2018. Remote sensing of plant-water relations: an overview and future perspectives. *J. Plant Physiol.* 227, 3–19. <https://doi.org/10.1016/j.jplph.2018.04.012>.
- Ershadi, A., McCabe, M.F., Evans, J.P., Walker, J.P., 2013. Effects of spatial aggregation on the multi-scale estimation of evapotranspiration. *Remote Sens. Environ.* 131, 51–62. <https://doi.org/10.1016/j.rse.2012.12.007>.
- Ershadi, A., McCabe, M.F., Evans, J.P., Chaney, N.W., Wood, E.F., 2014. Multi-site evaluation of terrestrial evaporation models using FLUXNET data. *Agric. For. Meteorol.* 187, 46–61. <https://doi.org/10.1016/j.agrformet.2013.11.008>.
- Fisher, J.B., Tu, K.P., Baldocchi, D.D., 2008. Global estimates of the land-atmosphere water flux based on monthly AVHRR and ISLSCP-II data, validated at 16 FLUXNET sites. *Remote Sens. Environ.* 112, 901–919. <https://doi.org/10.1016/j.rse.2007.06.025>.
- Fisher, J.B., Melton, F., Middleton, E., Hain, C., Anderson, M., Allen, R., McCabe, M., Hook, S., Baldocchi, D., Townsend, P.A., Kilic, A., Tu, K., Miralles, D., Perret, J., Lagouarde, J.-P., Waliser, D., Purdy, A.J., French, A., Schimel, D., Famiglietti, J.S., Stephens, G., Wood, E.F., 2017. The future of evapotranspiration: global requirements for ecosystem functioning, carbon and climate feedbacks, agricultural management, and water resources. *Water Resour. Res.* <https://doi.org/10.1002/2016WR020175>.
- Foley, J.A., Prentice, I.C., Ramankutty, N., Levis, S., Pollard, D., Sitch, S., Haxeltine, A., 1996. An integrated biosphere model of land surface processes, terrestrial carbon balance, and vegetation dynamics. *Glob. Biogeochem. Cycles* 10, 603–628. <https://doi.org/10.1029/96gb02692>.
- Fratini, G., Ibrom, A., Arriga, N., Burba, G., Papale, D., 2012. Relative humidity effects on water vapour fluxes measured with closed-path eddy-covariance systems with short sampling lines. *Agric. For. Meteorol.* 165, 53–63. <https://doi.org/10.1016/j.agrformet.2012.05.018>.
- Gago, J., Douthe, C., Coopman, R.E., Gallego, P.P., Ribas-Carbo, M., Flexas, J., Escalona, J., Medrano, H., 2015. UAVs challenge to assess water stress for sustainable agriculture. *Agric. Water Manag.* <https://doi.org/10.1016/j.agwat.2015.01.020>.
- Gamon, J.A., Penuelas, J., Field, C.B., 1992. A narrow-waveband spectral index that tracks diurnal changes in photosynthetic efficiency. *Remote Sens. Environ.* 41, 35–44. [https://doi.org/10.1016/0034-4257\(92\)90059-S](https://doi.org/10.1016/0034-4257(92)90059-S).
- GAO, W., 1995. Parameterization of subgrid-scale land-surface fluxes with emphasis on distributing mean atmospheric forcing and using satellite-derived vegetation index. *J. Geophys. Res.* 100, 14305–14317. <https://doi.org/10.1029/95jd01464>.
- García, M., Sandholt, I., Ceccato, P., Ridler, M., Mougín, E., Kergoat, L., Morillas, L., Timouk, F., Fensholt, R., Domingo, F., 2013. Actual evapotranspiration in drylands derived from in-situ and satellite data: assessing biophysical constraints. *Remote Sens. Environ.* 131, 103–118. <https://doi.org/10.1016/j.rse.2012.12.016>.
- García, M., Fernández, N., Villagarcía, L., Domingo, F., Puigdefábregas, J., Sandholt, I., 2014. Accuracy of the Temperature-Vegetation Dryness Index using MODIS under water-limited vs. energy-limited evapotranspiration conditions. *Remote Sens. Environ.* 149, 100–117. <https://doi.org/10.1016/j.rse.2014.04.002>.
- Garrigues, S., Allard, D., Baret, F., Weiss, M., 2006. Quantifying spatial heterogeneity at the landscape scale using variogram models. *Remote Sens. Environ.* 103, 81–96. <https://doi.org/10.1016/j.rse.2006.03.013>.
- Gentine, P., Entekhabi, D., Chehbouni, A., Boulet, G., Duchemin, B., 2007. Analysis of evaporative fraction diurnal behaviour. *Agric. For. Meteorol.* <https://doi.org/10.1016/j.agrformet.2006.11.002>.
- Gitelson, A.A., Vña, A., Arkebauer, T.J., Rundquist, D.C., Keydan, G., Leavitt, B., 2003. Remote estimation of leaf area index and green leaf biomass in maize canopies. *Geophys. Res. Lett.* 30 <https://doi.org/10.1029/2002GL016450>. n/a-n/a.
- Guan, K., Pan, M., Li, H., Wolf, A., Wu, J., Medvigy, D., Caylor, K.K., Sheffield, J., Wood, E.F., Malhi, Y., Liang, M., Kimball, J.S., Saleska, S.R., Berry, J., Joiner, J., Lyapustin, A.I., 2015. Photosynthetic seasonality of global tropical forests constrained by hydroclimate. *Nat. Geosci.* 8, 284–289. <https://doi.org/10.1038/ngeo2382>. <http://www.nature.com/ngeo/journal/v8/n4/abs/ngeo2382.html#supplementary-information>.
- Hoffmann, H., Nieto, H., Jensen, R., Guzinski, R., Zarco-Tejada, P., Friberg, T., 2016. Estimating evaporation with thermal UAV data and two-source energy balance models. *Hydrol. Earth Syst. Sci.* 20, 697–713. <https://doi.org/10.5194/hess-20-697-2016>.
- Houborg, R., Anderson, M.C., Norman, J.M., Wilson, T., Meyers, T., 2009.

- Intercomparison of a “bottom-up” and “top-down” modeling paradigm for estimating carbon and energy fluxes over a variety of vegetative regimes across the U.S. *Agric. For. Meteorol.* 149, 2162–2182. <https://doi.org/10.1016/j.agrformet.2009.10.002>.
- Huete, A.R., 1988. A soil-adjusted vegetation index (SAVI). *Remote Sens. Environ.* 25, 295–309. [https://doi.org/10.1016/0034-4257\(88\)90106-X](https://doi.org/10.1016/0034-4257(88)90106-X).
- Hulley, G.C., Hughes, C.G., Hook, S.J., 2012. Quantifying uncertainties in land surface temperature and emissivity retrievals from ASTER and MODIS thermal infrared data. *J. Geophys. Res. Atmos.* 117. <https://doi.org/10.1029/2012JD018506>.
- Ibrom, A., Dellwik, E., Flyvbjerg, H., Jensen, N.O., Pilegaard, K., 2007. Strong low-pass filtering effects on water vapour flux measurements with closed-path eddy correlation systems. *Agric. For. Meteorol.* 147, 140–156. <https://doi.org/10.1016/j.agrformet.2007.07.007>.
- Ibrom, A., Olchev, A., June, T., Kreilein, H., Rakkibu, G., Ross, T., Panferov, O., Gravenhorst, G., 2008. Variation in photosynthetic light-use efficiency in a mountainous tropical rain forest in Indonesia. *Tree Physiol.* 499–508. <https://doi.org/10.1093/treephys/28.4.499>.
- Ito, A., Inatomi, M., 2012. Water-use efficiency of the terrestrial biosphere: a model analysis focusing on interactions between the global carbon and water cycles. *J. Hydrometeorol.* 13, 681–694. <https://doi.org/10.1175/JHM-D-10-05034.1>.
- Kim, J., Guo, Q., Baldocchi, D.D., Leclerc, M.Y., Xu, L., Schmid, H.P., 2006. Upscaling fluxes from tower to landscape: overlaying flux footprints on high-resolution (IKONOS) images of vegetation cover. *Agric. For. Meteorol.* 136, 132–146. <https://doi.org/10.1016/j.agrformet.2004.11.015>.
- Kljun, N., Calanca, P., Rotach, M.W., Schmid, H.P., 2015. The simple two-dimensional parameterisation for Flux Footprint Predictions (FFP). *Geosci. Model Dev. Discuss.* 8, 6757–6808. <https://doi.org/10.5194/gmd-8-6757-2015>.
- Knauer, J., Zaehle, S., Medlyn, B.E., Reichstein, M., Williams, C.A., Migliavacca, M., De Kauwe, M.G., Werner, C., Keitel, C., Kolari, P., Limousin, J.M., Linderson, M.L., 2018. Towards physiologically meaningful water-use efficiency estimates from eddy covariance data. *Glob. Chang. Biol.* 24, 694–710. <https://doi.org/10.1111/gcb.13893>.
- Korpela, I., Heikkinen, V., Honkavaara, E., Rohrbach, F., Tokola, T., 2011. Variation and directional anisotropy of reflectance at the crown scale - implications for tree species classification in digital aerial images. *Remote Sens. Environ.* 115, 2062–2074. <https://doi.org/10.1016/j.rse.2011.04.008>.
- Kustas, W.P., Daughtry, C.S.T., 1990. Estimation of the soil heat flux/net radiation ratio from spectral data. *Agric. For. Meteorol.* 49, 205–223. [https://doi.org/10.1016/0168-1923\(90\)90033-3](https://doi.org/10.1016/0168-1923(90)90033-3).
- Kustas, W.P., Norman, J.M., 1999. Evaluation of soil and vegetation heat flux predictions using a simple two-source model with radiometric temperatures for partial canopy cover. *Agric. For. Meteorol.* 94, 13–29. [https://doi.org/10.1016/S0168-1923\(99\)00005-2](https://doi.org/10.1016/S0168-1923(99)00005-2).
- Kustas, W.P., Anderson, M.C., Alfieri, J.G., Knipper, K., Torres-Rua, A., Parry, C.K., Hieto, H., Agam, N., White, A., Gao, F., McKee, L., Prueger, J.H., Hipps, L.E., Los, S., Alsina, M., Sanchez, L., Sams, B., Dokoostlian, N., McKee, M., Jones, S., Yang, Y., Wilson, T.G., Lei, F., McElrone, A., Heitman, J.L., Howard, A.M., Post, K., Melton, F., Hain, C., 2018. The Grape Remote sensing Atmospheric Profile and Evapotranspiration Experiment (GRAPEX). *Bull. Am. Meteorol. Soc.* <https://doi.org/10.1175/BAMS-D-16-0244.1>. BAMS-D-16-0244.1.
- Larsen, M.A.D., Refsgaard, J.C., Jensen, K.H., Butts, M.B., Stisen, S., Mollerup, M., 2016. Calibration of a distributed hydrology and land surface model using energy flux measurements. *Agric. For. Meteorol.* 217, 74–88. <https://doi.org/10.1016/j.agrformet.2015.11.012>.
- Li, X., Cheng, G., Liu, S., Xiao, Q., Ma, M., Jin, R., Che, T., Liu, Q., Wang, W., Qi, Y., Wen, J., Li, H., Zhu, G., Guo, J., Ran, Y., Wang, S., Zhu, Z., Zhou, J., Hu, X., Xu, Z., 2013. Heihe watershed allied telemetry experimental research (HiWater) scientific objectives and experimental design. *Bull. Am. Meteorol. Soc.* 94, 1145–1160. <https://doi.org/10.1175/BAMS-D-12-00154.1>.
- Liu, Y., Xiao, J., Ju, W., Zhou, Y., Wang, S., 2015. Water use efficiency of China's terrestrial ecosystems and responses to drought. *Nat. Publ. Gr.* 1–12. <https://doi.org/10.1038/srep13799>.
- Malbêteau, Y., Parkes, S., Aragon, B., Rosas, J., McCabe, M., 2018. Capturing the diurnal cycle of land surface temperature using an unmanned aerial vehicle. *Remote Sens.* 10, 1407.
- McCabe, M.F., Wood, E.F., 2006. Scale influences on the remote estimation of evapotranspiration using multiple satellite sensors. *Remote Sens. Environ.* 105, 271–285. <https://doi.org/10.1016/j.rse.2006.07.006>.
- McCabe, M.F., Rodell, M., Alsdorf, D.E., Miralles, D.G., Uijlenhoet, R., Wagner, W., Lucier, A., Houborg, R., Verhoest, N.E.C., Franz, T.E., Shi, J., Gao, H., Wood, E.F., 2017. The future of Earth observation in hydrology. *Hydrol. Earth Syst. Sci.* 21, 3879–3914. <https://doi.org/10.5194/hess-21-3879-2017>.
- Metzger, S., 2018. Surface-atmosphere exchange in a box: making the control volume a suitable representation for in-situ observations. *Agric. For. Meteorol.* 255, 68–80. <https://doi.org/10.1016/j.agrformet.2017.08.037>.
- Mo, X., Liu, S., Lin, Z., Wang, S., Hu, S., 2014. Trends in land surface evapotranspiration across China with remotely sensed NDVI and climatological data for 1981–2010. *Hydrol. Sci. J.* 140917054829006. <https://doi.org/10.1080/02626667.2014.950579>.
- Mo, X., Liu, S., Chen, X., Hu, S., 2018. Variability, tendencies, and climate controls of terrestrial evapotranspiration and gross primary productivity in the recent decade over China. *Ecohydrology* 11. <https://doi.org/10.1002/eco.1951>.
- Moran, M.S., Clarke, T.R., Inoue, Y., Vidal, A., 1994. Estimating crop water deficit using the relation between surface-air temperature and spectral vegetation index. *Remote Sens. Environ.* 49, 246–263. [https://doi.org/10.1016/0034-4257\(94\)90020-5](https://doi.org/10.1016/0034-4257(94)90020-5).
- Morillas, L., Leuning, R., Villagarcía, L., García, M., Serrano-Ortiz, P., Domingo, F., 2013. Improving evapotranspiration estimates in Mediterranean drylands: the role of soil evaporation. *Water Resour. Res.* <https://doi.org/10.1002/wrcr.20468>. n/a–n/a.
- Morillas, L., Villagarcía, L., Domingo, F., Nieto, H., Uclés, O., García, M., 2014. Environmental factors affecting the accuracy of surface fluxes from a two-source model in Mediterranean drylands: upscaling instantaneous to daytime estimates. *Agric. For. Meteorol.* 189–190, 140–158. <https://doi.org/10.1016/j.agrformet.2014.01.018>.
- Mu, Q., Heinsch, F.A., Zhao, M., Running, S.W., 2007. Development of a global evapotranspiration algorithm based on MODIS and global meteorology data. *Remote Sens. Environ.* 111, 519–536. <https://doi.org/10.1016/j.rse.2007.04.015>.
- Ortega-Farías, S., Ortega-Salazar, S., Poblete, T., Kilic, A., Allen, R., Poblete-Echeverría, C., Ahumada-Orellana, L., Zuñiga, M., Sepúlveda, D., 2016. Estimation of energy balance components over a drip-irrigated olive orchard using thermal and multi-spectral cameras placed on a helicopter-based unmanned aerial vehicle (UAV). *Remote Sens.* 8, 1–18. <https://doi.org/10.3390/rs8080638>.
- Pilegaard, K., Ibrom, A., Courtney, M.S., Hummelshøj, P., Jensen, N.O., 2011. Increasing net CO<sub>2</sub> uptake by a Danish beech forest during the period from 1996 to 2009. *Agric. For. Meteorol.* 151, 934–946. <https://doi.org/10.1016/j.agrformet.2011.02.013>.
- Potter, C.S., Randerson, J.T., Field, C.B., Matson, P.A., Vitousek, P.M., Mooney, H.A., Klooster, S.A., 1993. Terrestrial ecosystem production: a process model based on global satellite and surface data. *Glob. Biogeochem. Cycles* 7, 811–841. <https://doi.org/10.1029/93GB02725>.
- Prata, A.J., 1996. A new long-wave formula for estimating downward clear-sky radiation at the surface. *Q. J. R. Meteorol. Soc.* 122, 1127–1151. <https://doi.org/10.1256/smsqj.53305>.
- Priestley, C., Taylor, R., 1972. On the assessment of surface heat flux and evaporation using large-scale parameters. *Mon. Weather Rev.* 81–92. [https://doi.org/10.1175/1520-0493\(1972\)100<0081:OTAOSH>2.3.CO;2](https://doi.org/10.1175/1520-0493(1972)100<0081:OTAOSH>2.3.CO;2).
- Propastin, P., Ibrom, A., Knohl, A., Erasmí, S., 2012. Effects of canopy photosynthesis saturation on the estimation of gross primary productivity from MODIS data in a tropical forest. *Remote Sens. Environ.* 121, 252–260. <https://doi.org/10.1016/j.rse.2012.02.005>.
- Rahman, A.F., Gamon, J.A., Sims, D.A., Schmidts, M., 2003. Optimum pixel size for hyperspectral studies of ecosystem function in southern California chaparral and grassland. *Remote Sens. Environ.* 84, 192–207. [https://doi.org/10.1016/S0034-4257\(02\)00107-4](https://doi.org/10.1016/S0034-4257(02)00107-4).
- Reichstein, M., Falge, E., Baldocchi, D., Papale, D., Aubinet, M., Berbigier, P., Bernhofer, C., Buchmann, N., Gilmanov, T., Granier, A., Grünwald, T., Havránková, K., Ivesniemi, H., Janous, D., Knohl, A., Laurila, T., Lohila, A., Loustau, D., Matteucci, G., Meyers, T., Miglietta, F., Ourcival, J.M., Pumpanen, J., Rambal, S., Rotenberg, E., Sanz, M., Tenhunen, J., Seufert, G., Vaccari, F., Vesala, T., Yakir, D., Valentini, R., 2005. On the separation of net ecosystem exchange into assimilation and ecosystem respiration: review and improved algorithm. *Glob. Chang. Biol.* <https://doi.org/10.1111/j.1365-2486.2005.001002.x>.
- Running, S.W., Nemani, R.R., Heinsch, F.A.N.N., Zhao, M., Reeves, M., Hashimoto, H., 2004. A continuous satellite-derived measure of global terrestrial primary production. *Bioscience* 54, 547. [https://doi.org/10.1641/0006-3568\(2004\)054](https://doi.org/10.1641/0006-3568(2004)054).
- Sabol, D.E., Gillespie, A.R., Abbott, E., Yamada, G., 2009. Field validation of the ASTER Temperature-Emissivity Separation algorithm. *Remote Sens. Environ.* 113, 2328–2344. <https://doi.org/10.1016/j.rse.2009.06.008>.
- Sharma, V., Kilic, A., Irmak, S., 2016. Impact of scale/resolution on evapotranspiration from Landsat and MODIS images. *Water Resour. Res.* 52, 1800–1819. <https://doi.org/10.1002/2015WR017772>.
- Sitch, S., Prentice, I.C., Arneth, A., Cramer, W., Kaplan, J.O., Levis, S., Lucht, W., Sykes, M.T., Thonicke, K., 2003. Evaluation of ecosystem dynamics, plant geography and terrestrial carbon cycling in the LPJ dynamic global vegetation model. *Glob. Chang. Biol.* 9, 161–185. <https://doi.org/10.1046/j.1365-2486.2003.00569.x>.
- Twine, T.E., Kustas, W.P., Norman, J.M., Cook, D.R., Houser, P.R., Meyers, T.P., Prueger, J.H., Starks, P.J., Wesely, M.L., 2000. Correcting eddy-covariance flux underestimates over a grassland. *Agric. For. Meteorol.* 103, 279–300. [https://doi.org/10.1016/S0168-1923\(00\)00123-4](https://doi.org/10.1016/S0168-1923(00)00123-4).
- Van de Griend, M., Owe, A.A., 1993. On the relationship between thermal emissivity and normalized vegetation index for natural surfaces. *Int. J. Remote Sens.* 14, 1119–1131. <https://doi.org/10.1080/01431169308904400>.
- Viña, A., Gitelson, A.A., Nguy-Robertson, A.L., Peng, Y., 2011. Comparison of different vegetation indices for the remote assessment of green leaf area index of crops. *Remote Sens. Environ.* 115, 3468–3478. <https://doi.org/10.1016/j.rse.2011.08.010>.
- Vivoni, E.R., Rango, A., Anderson, C.A., Pierini, N.A., Schreiner-McGraw, A.P., Saripalli, S., Laliberte, A.S., 2014. Ecohydrology with unmanned aerial vehicles. *Ecosphere* 5, art130. <https://doi.org/10.1890/ES14-00217.1>.
- Wang, S., Dam-Hansen, C., Zarco Tejada, P.J., Thorseth, A., Malureanu, R., Bandini, F., Jakobsen, J., Ibrom, A., Bauer-Gottwein, P., Garcia, M., 2017. Optimizing sensitivity of Unmanned Aerial System optical sensors for low zenith angles and cloudy conditions. In: Poster Session Presented at 10th EARSeL SIG Imaging Spectroscopy Workshop, Zurich, Switzerland. 10th EARSeL SIG Imaging Spectrosc. Work. - Zurich, Switz. 2017.
- Wang, S., Garcia, M., Ibrom, A., Jakobsen, J., Josef Köppl, C., Mallick, K., Looms, M., Bauer-Gottwein, P., 2018a. Mapping root-zone soil moisture using a temperature–vegetation triangle approach with an unmanned aerial system: incorporating surface roughness from structure from motion. *Remote Sens.* 10, 1978.
- Wang, S., Ibrom, A., Bauer-Gottwein, P., Garcia, M., 2018b. Incorporating diffuse radiation into a light use efficiency and evapotranspiration model: an 11-year study in a high latitude deciduous forest. *Agric. For. Meteorol.* 248, 479–493. <https://doi.org/10.1016/j.agrformet.2017.10.023>.
- Westoby, M.J., Brasington, J., Glasser, N.F., Hambrey, M.J., Reynolds, J.M., 2012. “Structure-from-Motion” photogrammetry: a low-cost, effective tool for geoscience applications. *Geomorphology* 179, 300–314. <https://doi.org/10.1016/j.geomorph.2012.08.021>.

- Wutzler, T., Lucas-Moffat, A., Migliavacca, M., Knauer, J., Sickel, K., Šigut, L., Menzer, O., Reichstein, M., 2018. Basic and extensible post-processing of eddy covariance flux data with REddyProc. *Biogeosciences* 15, 5015–5030. <https://doi.org/10.5194/bg-15-5015-2018>.
- Yu, X., Liu, Q., Liu, X., Liu, X., Wang, Y., 2016. A physical-based atmospheric correction algorithm of unmanned aerial vehicles images and its utility analysis. *Int. J. Remote Sens.* 1–12. <https://doi.org/10.1080/01431161.2016.1230291>.
- Zarco-Tejada, P.J., González-Dugo, V., Williams, L.E., Suárez, L., Berni, J.A.J., Goldammer, D., Fereres, E., 2013a. A PRI-based water stress index combining structural and chlorophyll effects: assessment using diurnal narrow-band airborne imagery and the CWSI thermal index. *Remote Sens. Environ.* 138, 38–50. <https://doi.org/10.1016/j.rse.2013.07.024>.
- Zarco-Tejada, P.J., Morales, A., Testi, L., Villalobos, F.J., 2013b. Spatio-temporal patterns of chlorophyll fluorescence and physiological and structural indices acquired from hyperspectral imagery as compared with carbon fluxes measured with eddy covariance. *Remote Sens. Environ.* 133, 102–115. <https://doi.org/10.1016/j.rse.2013.02.003>.
- Zhang, C., Filella, I., Garbulsky, M.F., Peñuelas, J., 2016. Affecting factors and recent improvements of the photochemical reflectance index (PRI) for remotely sensing foliar, canopy and ecosystemic radiation-use efficiencies. *Remote Sens.* <https://doi.org/10.3390/rs8090677>.
- Zhang, Q.M., Chen, J., Ju, W., Wang, H., Qiu, F., Yang, F., Fan, W., Huang, Q., Wang, Y. ping, Feng, Y., Wang, X., Zhang, F., 2017. Improving the ability of the photochemical reflectance index to track canopy light use efficiency through differentiating sunlit and shaded leaves. *Remote Sens. Environ.* 194, 1–15. <https://doi.org/10.1016/j.rse.2017.03.012>.
- Zhu, W., Jia, S., Lv, A., 2017. A time domain solution of the Modified Temperature Vegetation Dryness Index (MTVDI) for continuous soil moisture monitoring. *Remote Sens. Environ.* 200, 1–17. <https://doi.org/10.1016/j.rse.2017.07.032>.